GENETICS

Widespread association of Polycomb complex–deposited histone H2A monoubiquitylation with enhancers and neuronal gene regulation

Kailynn MacGillivray†, Daniel Fusca†‡, Luomeng Tan, Reta Aram, Arneet L. Saltzman*

Disruption of histone H2A monoubiquitylation (H2AK119ub) causes neurodevelopmental disorders through poorly understood mechanisms. Polycomb complex–deposited H2AK119ub and trimethylation of histone H3 at lysine 27 (H3K27me3) can cooperatively maintain gene repression. However, the extent to which H2AK119ub functions independently of H3K27me3 to repress or potentiate gene expression, and the evolutionary conservation of these roles, remains unclear. Here, we address the interplay among Polycomb-deposited marks and chromatin states in *Caenorhabditis elegans* embryos. We find that H2AK119ub distribution is distinct from and largely dispensable for H3K27me3 patterns. Unexpectedly, H2AK119ub is enriched at predicted enhancers with developmentally dynamic changes in accessibility, including in neurons. More than two-thirds of well-documented axon guidance genes and neuronal identity transcription factors are associated with H2AK119ub. Many of the genes differentially expressed in H2AK119ub-deficient animals are involved in neuronal differentiation and signaling and feature H2AK119ub-enriched promoters and enhancers, including a subset that is H3K27me3 repressed. We uncover a likely conserved yet underappreciated dual role for H2AK119ub at enhancers and H3K27me3-repressed chromatin, with implications for nervous system development.

INTRODUCTION

Polycomb repressive complexes are major regulators of chromatin state and gene expression. Polycomb proteins can be grouped into two families of multisubunit complexes, Polycomb repressive complex 2 (PRC2), which is responsible for trimethylation of histone H3 at lysine 27 (H3K27me3), and Polycomb repressive complex 1 (PRC1), which is responsible for monoubiquitylation of histone H2AK119 (H2AK119ub) (*1*). PRC1 complexes can be further subdivided into canonical PRC1 (cPRC1) and variant PRC1 (vPRC1) based on their subunits and mechanism of genomic targeting (*1–3*). In cPRC1, a chromobox (CBX) protein subunit binds H3K27me3 via its chromodomain (*1, 3–5*). In vPRC1, RING1 and YY1 binding protein (RYBP) replaces the CBX subunit, and therefore targeting of this complex can be independent of H3K27me3 (*1, 2, 6, 7*). vPRC1 complexes are responsible for most H2AK119ub in vivo, potentially due to the ability of RYBP to stimulate ubiquitylation activity (*7–10*). While the interaction between cPRC1 and H3K27me3 is well established, the relationship between vPRC1-deposited H2AK119ub and H3K27me3 is less well understood.

PRC1 activity has different impacts on gene expression depending on the context. PRC1 can induce H3K27me3-independent gene silencing via inhibition of Ser^5-phosphorylated RNA polymerase II association with transcription start sites (*11*). PRC1 can also function cooperatively and redundantly with PRC2 and H3K27me3 to mediate target gene repression (*12–15*). cPRC1-associated gene repression can be mediated by H2AK119ub-independent chromatin compaction (*16, 17*), but accumulation of H2AK119ub increases DNA accessibility at target sites (*18*). vPRC1 can also promote the expression of transcription factors in epidermal differentiation (*12*). In addition,

cPRC1 components, including Sce (sex combs extra)/RING1B, Psc/PCGF2,4 (posterior sex combs/Polycomb group ring finger 2, 4), Pc (Polycomb)/CBX, and Ph/PHC (polyhomeotic/polyhomeotic homolog 1), occupy promoter and/or enhancer regions in *Drosophila* eye-antennal imaginal discs, mouse neural progenitor cells (NPCs), and mammalian cancer cell lines, and their binding correlates with increased expression of the associated genes and higher enhancer-promoter contact frequencies (*19–22*). Although the involvement of PRC1 in both gene repression and gene activation has been demonstrated, the role of H2AK119ub in each process is unresolved.

PRC1 activity is a critical regulator of neuronal development (*23*). In mammals, loss of RING1B or BMI1 (BMI1 proto-oncogene, Polycomb ring finger)/PCGF4 results in defects in self-renewal and differentiation capacity of embryonic neural stem cells and early NPCs (*24, 25*). The PRC1 complex is thought to inhibit neuronal differentiation in multipotent cell types by maintaining neuronal-lineage genes in a poised state, a process that is impeded by reduction of H2AK119ub (*23–27*). As NPCs differentiate, H2AK119ub-independent PRC1 compaction activity is critical for repression of nonlineage genes and specification of spinal motor neuron subtypes (*24, 28*). RING1B is also important for dorsoventral patterning of the mouse brain by repression of bone morphogenetic protein and WNT signaling (*29*). Whether these functions in neuronal development and regulatory mechanisms are conserved between species and their roles in the pathogenesis of PRC1-dependent neurodevelopmental disorders (*30*) are unknown.

In *Caenorhabditis elegans*, the PRC1-like and PRC2 complexes are associated with mostly distinct developmental and fertility phenotypes. Mutations in *mig-32* or *spat-3*, the putative functional homologs of the core PRC1 components, PCGF and RING1A/B, respectively, greatly reduce levels of H2AK119ub (*31, 32*). The mammalian numbering will be used for consistency here, although K119 in mammalian H2A corresponds to K120 in *C. elegans* histone H2A (fig. S1). These mutant animals also have neuronal development defects, including defective migration, axon guidance, and posterior process termination of the hermaphrodite-specific motor neurons (HSNs), posterior ventral

Department of Cell and Systems Biology, University of Toronto, Toronto, ON, Canada.
*Corresponding author. Email: arneet.saltzman@utoronto.ca
†These authors contributed equally to this work.
‡Present address: Department of Ecology and Evolutionary Biology, University of Toronto, Toronto, ON, Canada.

process Q (PVQ) neurons, and posterior lateral microtubule (PLM) neurons, respectively (*31*, *32*). Furthermore, *mig-32* and *spat-3* mutants have defects in specification and maintenance of AIY cholinergic interneuron cell fate, likely due to misregulation of key transcription factors (*33*). These phenotypes support the importance of PRC1 activity in neuronal development and gene regulation; however, the direct mechanisms of these neuronal phenotypes are not well understood. In contrast, neuronal development defects have not been observed in mutants for the *C. elegans* PRC2 complex, composed of MES-2/EZH1/2 (maternal effect sterile 2/enhancer of zeste homolog 1/2), MES-3/SUZ12 (SUppressor of zeste 12), and MES-6/EED (embryonic ectoderm development) (*34*). The *C. elegans* PRC2 complex is involved in *Hox* gene silencing and repression of transition genes in late embryos (*35*, *36*). Its key role in maintaining germ cell identity and gene expression leads to a characteristic Mes phenotype in PRC2 mutants (*37*, *38*). In contrast, there is currently no evidence for the involvement of the PRC1-like complex in these processes, as *mig-32* and *spat-3* mutant animals are fertile. However, both the PRC1-like and PRC2 complexes do act in the same genetic pathway to regulate male tail morphogenesis (*31*, *35*). Together, these phenotypes suggest that PRC1 and PRC2 play at least partially independent roles in *C. elegans* development. However, the target genes regulated by the *C. elegans* PRC1-like complex have not been identified, and it remains unclear to what extent these two complexes are functioning cooperatively or independently on a genome-wide level.

Here, we present a global analysis of Polycomb-associated histone H2AK119ub in *C. elegans*, capturing the embryonic stage at which the PRC1 component homologs are most highly expressed (*39*, *40*). We find that, in contrast to mammals and *Drosophila* (*10*, *41*, *42*), a substantial proportion of H2AK119ub is distinct from H3K27me3 and that overall H3K27me3 patterns are maintained when H2AK119ub is depleted. Unexpectedly, H2AK119ub is enriched at enhancer chromatin states and shows a conserved overlap with enhancer-associated monomethylation of histone H3 at lysine 4 (H3K4me1). Furthermore, H2AK119ub is enriched at enhancers that gain accessibility in neurons later during development. Genes misregulated in H2AK119ub-deficient mutants are enriched for nervous system functions, and H2AK119ub-enriched genes show widespread overlap with well-characterized axon guidance genes and most transcription factors required for neuron type–specific cell fate. Our results reveal pathways likely to underlie the functional importance of H2AK119ub in neuronal development and suggest a conserved regulatory role for PRC1 in enhancer regulation.

RESULTS

Genome-wide patterns of H2AK119ub and H3K27me3 are mostly distinct in *C. elegans* embryos

To investigate the relationship between H2AK119ub and H3K27me3 in *C. elegans*, we performed chromatin immunoprecipitation sequencing (ChIP-seq) for both histone modifications in embryos and examined their genomic distributions (Fig. 1, figs. S1 and S2, and tables S1 and S2). In contrast to the coenrichment of PRC1, PRC2, and their histone marks, which has been previously observed in mouse embryonic stem cells, mammalian epidermal progenitor cells, and *Drosophila* (*12*, *43*, *44*), a comparison of the consensus peaks called in two biological replicates (fig. S1) revealed two classes of H2AK119ub peaks based on their overlap with H3K27me3 (Fig. 1A, clusters 1 and 2). The overlapping genome coverage of the two peak sets represents ~32 and 19% of the H2AK119ub and H3K27me3 peak sets, respectively (Fig. 1B, top). When quantifying the overlapping peaks, 10 to 40% of the peaks overlap, depending on the stringency of the comparison (Fig. 1B, bottom). Upon examining their distributions over whole chromosomes, H3K27me3 is enriched at the heterochromatin-rich chromosome arms (Fig. 1C and fig. S3), as previously described (*45*), particularly the arms of chromosome II and chromosome V. However, unexpectedly and in contrast to H3K27me3, H2AK119ub is not enriched on the heterochromatic arms. These peak and distribution patterns suggest that PRC1-mediated H2AK119ub has functions that are separate from H3K27me3-marked heterochromatin and Polycomb domains.

To compare the enrichment patterns of H2AK119ub with other histone modifications, we used embryonic ChIP-seq data from the modENCODE consortium (table S2) (*46*), computed pairwise Spearman correlation coefficients for coverage across the genome (Fig. 1D), and compared enrichment across chromosomes (fig. S3). On a genome-wide scale, the heterochromatin-associated marks H3K27me3 and H3K9me3 are highly correlated, as previously described (*46*), while H2AK119ub has a very-weak overall correlation with H3K27me3 (Fig. 1D). Instead, H2AK119ub is positively correlated with H3K4me1 (Fig. 1D), a mark associated with enhancers and promoters (*46–48*), and with monomethylation of histone H4 at lysine 20 (H4K20me1), a mark enriched on the X chromosome (fig. S3) by the dosage compensation complex (DCC) (*49–52*). Notably, although the PRC1-like complex has not been previously implicated in dosage compensation, H2AK119ub is unexpectedly enriched on the X chromosome (Fig. 1C and figs. S2 and S3), which likely accounts for its correlation with H4K20me1. Our results therefore suggest that H2AK119ub may play a role in X-chromosome regulation, potentially in conjunction with either PRC2-deposited H3K27me3 (*34*, *53*) or with the DCC. However, across the genome, H2AK119ub has a low correlation with H3K27me3, which suggests that these two histone modifications can play independent roles in gene regulation and are associated with distinct chromatin states.

Given the unexpected distribution of H2AK119ub, we investigated whether recognition of the monoubiquitylated form of the H2A variant H2A.Z (*C. elegans* HTZ-1; fig. S1A) in our ChIP-seq assays could account for this pattern (fig. S4). When comparing our H2AK119ub ChIP-seq with previously published HTZ-1 ChIP-seq (*54*), only 9% (551/6098) of H2AK119ub peaks overlap with HTZ-1 peaks (fig. S4). Furthermore, previous profiling revealed an enrichment of HTZ-1 across gene bodies (*55*), which is distinct from the distribution of H2AK119ub at upstream regions in our data (see below). This analysis supports that most of the H2AK119ub ChIP-seq signal is from H2AK119ub and not the ubiquitinated form of the HTZ-1. Therefore, we conclude that in *C. elegans* embryos, the global distribution of Polycomb-mediated H2AK119ub is largely distinct from heterochromatin-associated H3K27me3.

H2AK119ub is enriched at enhancer chromatin states

To further investigate genome-wide H2AK119ub patterns, we plotted the H2AK119ub ChIP-seq signal over two sets of hidden Markov model (HMM)–predicted chromatin states (Fig. 2A) (*56*, *57*). Unexpectedly, the H2AK119ub ChIP-seq signal is consistently highest, and peak coverage is significantly enriched at enhancer chromatin states, including predicted repressed and active enhancers, intergenic, intronic, and weak enhancers (Fig. 2 and fig. S5A). H2AK119ub
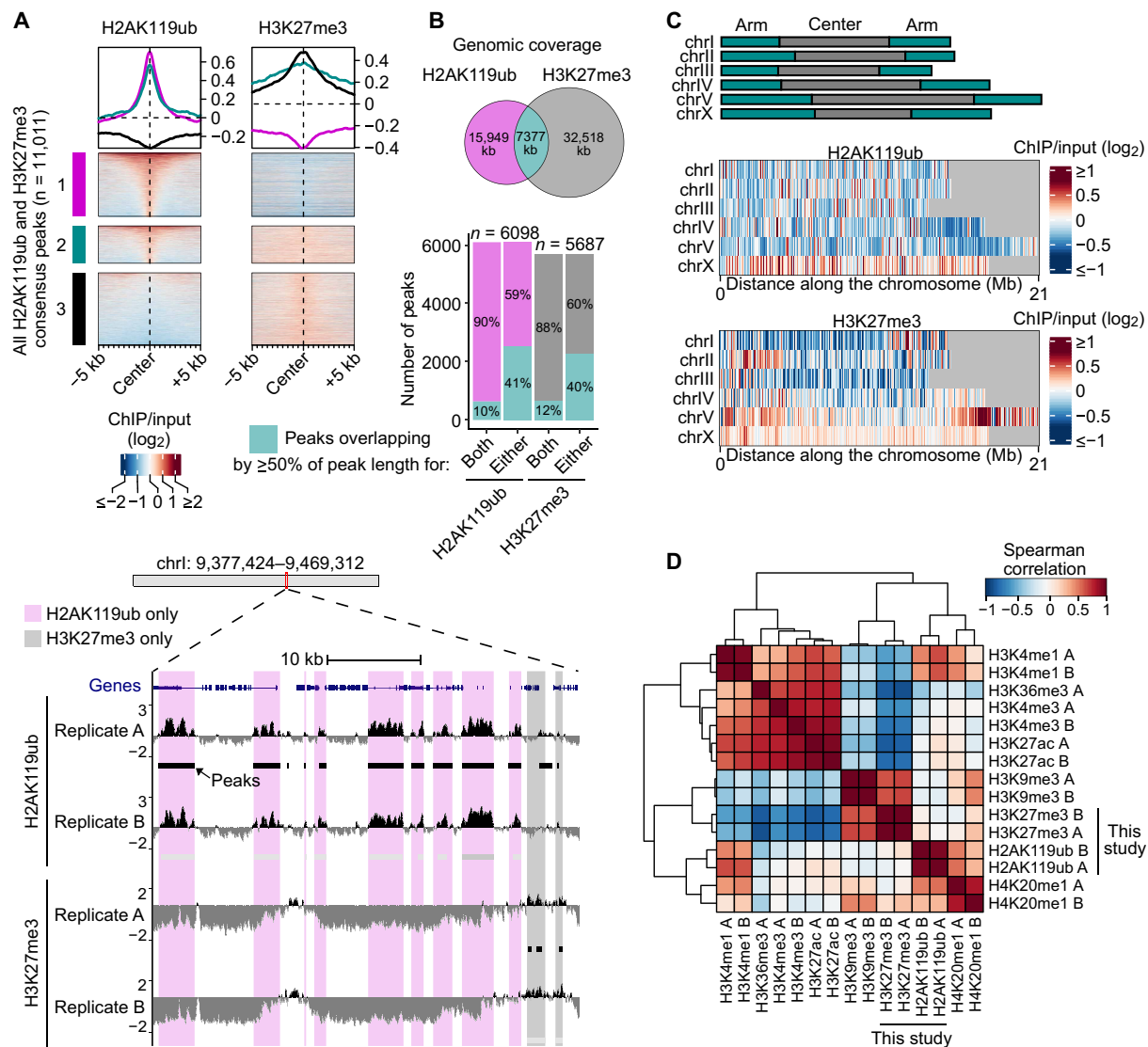
Fig. 1. H2AK119ub and H3K27me3 have partially distinct genomic distributions in *C. elegans* embryos. (**A**) Heatmaps of H2AK119ub and H3K27me3 ChIP-seq (log$_2$-transformed ChIP/input ratios) at all H2AK119ub and H3K27me3 consensus peaks. Consensus peaks are those called in two wild-type (N2) biological replicates. Peaks are organized into clusters, with cluster 2 containing the H2AK119ub and/or H3K27me3 peaks that have at least 50% of their peak lengths overlapping with the other histone modification. Cluster 1 and cluster 3 contain the H2AK119ub and H3K27me3 peaks, respectively, that do not satisfy this overlap requirement. Bottom: Representative UCSC Genome Browser tracks for two biological replicates showing distinct H2AK119ub and H3K27me3 peaks in the center region of chromosome I. For additional ge-nome browser tracks, see fig. S2. (**B**) Quantification of the overlap of H2AK119ub and H3K27me3 genome coverage (top panel) and consensus peaks (bottom panel). Peaks are called as overlapping if at least 50% of their peak region overlaps with the other histone modification. The required fraction of overlap can be reciprocal (both) or satisfied by either peak (either). See Materials and Methods for details. (**C**) Heatmaps of H2AK119ub and H3K27me3 ChIP-seq (log$_2$-transformed ChIP/input ratios) across whole *C. elegans* chromosomes. Scale represents average enrichment in 50-kb bins. The representative diagram indicates the positions of the arms and centers of each chromosome (top) (*130*). For additional replicates and histone modifications, see fig. S3. (**D**) Heatmap of the Spearman correlation coefficients for the distributions of dif-ferent histone modifications across all *C. elegans* chromosomes. Rows and columns are organized by hierarchical clustering. (A) and (B) indicate biological replicates.

peaks are also notably coenriched with H3K4me1 (Fig. 2C), which is consistent with the genome-wide correlation data (Fig. 1D) and, to a lesser extent, with histone H3 lysine 27 acetylation (H3K27ac). The positions of the predicted enhancers also correlate with H2AK119ub peak positions (Fig. 2C). Because H3K4me1 enrichment is found at both enhancers and promoters, we also determined the overlap of these chromatin state–predicted enhancers with a dataset that more stringently differentiated enhancers from promoters by the presence

of stable elongating transcription in the latter (*48, 58*). This analysis supports the interpretation that most of the chromatin state–predicted enhancers represent enhancers, whereas ~20% do overlap with pro-moters (fig. S5B). Given the compactness of the *C. elegans* genome, these overlapping states may also represent regions functioning as composite enhancer-promoter elements. These findings suggest that, similar to H3K4me1 and H3K27ac (*46, 47, 59, 60*), H2AK119ub is part of an enhancer chromatin signature.
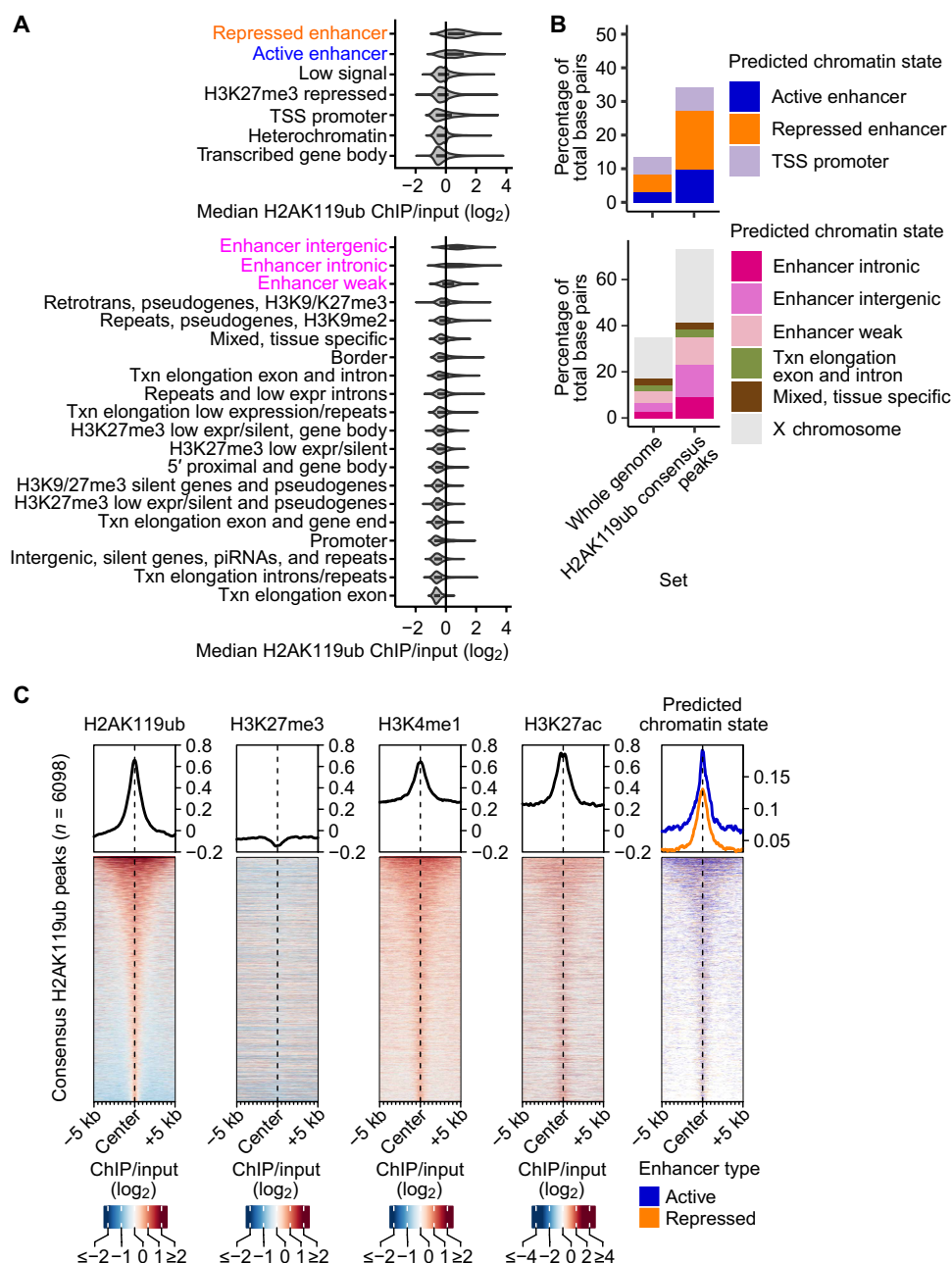
Fig. 2. H2AK119ub is enriched at enhancer-like domains. (**A**) Median H2AK119ub signal (log$_2$-transformed ChIP/input ratios) over chromatin state maps. The top panel includes seven HMM-predicted chromatin states based on eight histone modification ChIP-seq datasets (56). The bottom panel includes 20 HMM-predicted chromatin states based on 17 histone and histone modification ChIP-chip/ChIP-seq datasets (57). Chromatin states are arranged in order of decreasing H2AK119ub signal. TSS, transcription start site; expr, expression; piRNAs, Piwi-interacting RNAs. (**B**) Histone H2AK119ub peak coverage over predicted chromatin states described in (A) shows enrichment over enhancer states and on the X chromosome. All states with significant enrichment when compared to the genome ($P < 2.2 \times 10^{-16}$; Fisher's exact test) are shown. For the proportions of bases covered by all states and comparison to H3K27me3, see fig. S5. (**C**) Heatmaps of H2AK119ub, H3K27me3, H3K4me1, and H3K27ac (log$_2$-transformed ChIP/input ratios) and positions of active and repressed enhancer states (56) at H2AK119ub consensus peaks. N2 consensus peaks are those called in two H2AK119ub ChIP-seq biological replicates. H3K4me1 and H3K27ac data from modENCODE consortium (46).

To examine the relationship between H2AK119ub, H3K27me3, and H3K4me1 in published data from mammals, we clustered ChIP-seq peaks from mouse epidermal progenitor cells (12), the leukemia cell line K562 (61), and the breast cancer cell line T47D (fig. S5C) (20). In all three cell types, we observed a subset of H2AK119ub peaks that are coenriched with H3K27me3 (fig. S5C), which is consistent with the known cotargeting of repressed genes by PRC1 and PRC2 (12, 43). However, a third cluster of ~17 to 34% of H2AK119ub peaks with H3K4me1 coenrichment and relatively low H3K27me3 also emerges (fig. S5C). Together, these results suggest a conserved and potentially H3K27me3-independent role for H2AK119ub at H3K4me1-enriched regions, including enhancers.

H2AK119ub and H3K27me3 are not dependent on each other's presence

To investigate whether H2AK119ub and H3K27me3 are interdependent, we used Western blotting to determine the bulk levels of these histone marks in mutants of the PRC1 component homologs, *mig-32* and *spat-3*. The *mig-32(n4275)* allele is a deletion spanning the start of the coding region (*31*), and the *spat-3(mgw26)* allele (*32*) is a deletion of the entire coding region (fig. S6 and table S1). The *spat-3(gk22)* allele (*31*) is a deletion that does not overlap with the conserved RING domain (fig. S6B). As observed previously (*62, 63*), the H2AK119ub antibody detects a major monoubiquitylated H2A (H2Aub1) band and a second ~32-kDa band corresponding to H2Aub2, both of which are reduced in PRC1 mutants (Fig. 3A and fig. S7; see Materials and Methods) (*62*). In *spat-3(gk22)*, which is likely a partial loss of function, H2AK119ub is reduced to ~60% of wild-type levels. In *mig-32(n4275)*, *spat-3(mgw26)*, *mig-32(n4275);spat-3(gk22)*, and *mig-32(n4275);spat-3(mgw26)* mutants, H2AK119ub levels are markedly reduced to 2 to 5% of wild type (Fig. 3A and fig. S7). However, although H2AK119ub is severely depleted in the *mig-32(n4275)* and *spat-3(mgw26)* mutants, H3K27me3 levels are not reduced (Fig. 3A).

To determine whether this pattern is also observed at the level of peaks, we performed ChIP-seq in wild-type (N2) and *mig-32(n4275)* embryos. Consistent with the Western blots above, we see a strong loss of H2AK119ub signal and peaks in *mig-32* mutants in both standard and quantitative [exogenous chromatin spike-in normalized (*10, 64*)] ChIP-seq and in ChIP–quantitative polymerase chain reaction (qPCR) (Fig. 3 and figs. S1, S2, and S8). To identify reproducible peaks, we defined H2AK119ub consensus peak sets for each genotype as peaks called in at least two of four biological replicates (fig. S1D). When comparing the N2 and *mig-32* consensus peak sets, the majority (96%; 5516/5737) of H2AK119ub peaks called in N2 were lost in *mig-32(n4275)* mutants (Fig. 3B, top, and fig. S8C). For example, the H2AK119ub peak over the gene body of *snai-1* and *dsc-4* is lost in *mig-32(n4275)* mutants (Fig. 3C, top). The remaining 3.9% (221/5737) of H2AK119ub consensus peaks called in *mig-32(n4275)* animals were a subset of the N2 consensus peaks but were generally attenuated and substantially shorter in the mutants (Fig. 3B and fig. S8D), such as the peak in the gene body of *lin-11* and upstream of *ZC247.2* (Fig. 3C, middle). The reduction of H2AK119ub in *mig-32(n4275)* mutants was further validated by ChIP-qPCR at three representative peaks (fig. S8). The genes associated with the attenuated H2AK119ub peaks called in *mig-32(n4275)* mutants did not appear to be a functionally distinct subset of genes because they had similar Gene Ontology (GO) terms to the genes associated with H2AK119ub peaks in wild-type N2 animals (fig. S8E; see below). For N2 animals, the H2AK119ub peaks were similar in the spike-in–normalized and standard ChIP-seq replicates (Fig. 3B, top, and figs. S1D and S8C, left). However, for *mig-32* mutants, H2AK119ub coverage and peaks were highly reduced in spike-in–normalized (0 to 19 peaks per replicate) compared to standard ChIP-seq (411 to 955 peaks per replicate) (Fig. 3B and figs. S1, S2, and S8C). We conclude that, while low levels of H2AK119ub may remain in *mig-32* mutants, the signal of remaining H2AK119ub peaks called in nonnormalized ChIP-seq is overestimated by standard read-depth normalization.

In contrast to the loss of H2AK119ub, heatmaps of H3K27me3 peaks in N2 and *mig-32(n4275)* mutants are nearly indistinguishable, and the vast majority (71%; 4250/5957) of the N2 or *mig-32(n4275)* H3K27me3 consensus peaks, defined as peaks called in at least two of three biological replicates, are common to both N2 and

the *mig-32(n4275)* mutants (Fig. 3B, bottom, and figs. S1D and S8C, right). When comparing H3K27me3 signal in spike-in–normalized samples, the common peaks do not show an overall significant difference in H3K27me3 between the genotypes (fig. S9, A and B). The remaining H3K27me3 peaks that show reduced (14%; 854/5957) or increased (14%; 853/5957) signal in *mig-32(n4275)* mutants overlap with H2AK119ub at a similar frequency as the common peaks (24 to 36%; fig. S9A). Average coverage line plots also do not show a decrease in H3K27me3 in *mig-32* mutants for the subset of these peaks that overlap with H2AK119ub (fig. S9C). These results contrast with previous studies in other systems where loss of PRC1/vPRC1 components resulted in reduced H3K27me3 (*10, 41, 42*) and with the demonstrated role of vPRC1 and H2AK119ub in PRC2/H3K27me3 recruitment (*2, 65, 66*). With the caveat that *mig-32* mutants have greatly reduced but possibly not fully abolished H2AK119ub, in *C. elegans* embryos, *mig-32* and H2AK119ub may play a role at specific locations but are largely dispensable for the H3K27me3 genomic distribution.

To test whether the converse is also true, if H2AK119ub deposition depends on PRC2/H3K27me3, we used Western blotting to assess the levels of H2AK119ub and H3K27me3 following knockdown of *mes-2*, the *C. elegans* homolog of *E(z)*, the H3K27 methyltransferase of the *Drosophila* PRC2 complex (*34*). As expected, in embryos collected from adults exposed to *mes-2* RNA interference (RNAi), H3K27me3 is severely depleted (Fig. 3D). However, the levels of H2AK119ub are not disrupted (Fig. 3D), indicating that the bulk level of H2AK119ub is not dependent on the presence of H3K27me3. Together, these results suggest that the two histone modifications are predominantly regulated independently.

Distinct and common features of H2AK119ub- and H3K27me3-associated genes

To compare the features of H2AK119ub- and H3K27me3-associated genes, we examined the distribution of these modifications over all protein-coding genes and their flanking regions (Fig. 4 and table S3). In general, H2AK119ub is most enriched over upstream regions, whereas H3K27me3 enrichment extends from upstream to downstream regions, with the highest enrichment over the gene body (Fig. 4A). Of the protein-coding genes with associated H2AK119ub or H3K27me3 consensus peaks ($n = 7195$), only 20% ($n = 1412$) are annotated with both (Fig. 4B), which nevertheless represents a higher overlap than would be expected by chance ($P < 2.2 \times 10^{-16}$; Fisher's exact test). This gene set overlap analysis is consistent with the genome-wide patterns above (Fig. 1) and supports regulation of mostly distinct sets of genes, with a smaller subset of common targets.

Because H3K27me3 is associated with gene repression, we compared the enrichment of H3K27me3 and H2AK119ub upstream of protein-coding genes divided into quartiles of expression based on RNA sequencing (RNA-seq) data in N2 (wild-type) embryos (Fig. 4C). As expected, H3K27me3 is enriched upstream of silent and lowly expressed genes and is depleted upstream of genes in the highest quartiles of expression (Fig. 4C). In contrast, H2AK119ub does not show this pattern and is not enriched at lowly expressed or silent genes (Fig. 4C). Thus, H2AK119ub shows less association with gene repression than H3K27me3, which is consistent with the low enrichment of H2AK119ub at heterochromatin and other repressed chromatin states (Fig. 2 and fig. S5) and suggests that these two histone modifications play distinct roles in gene regulation.
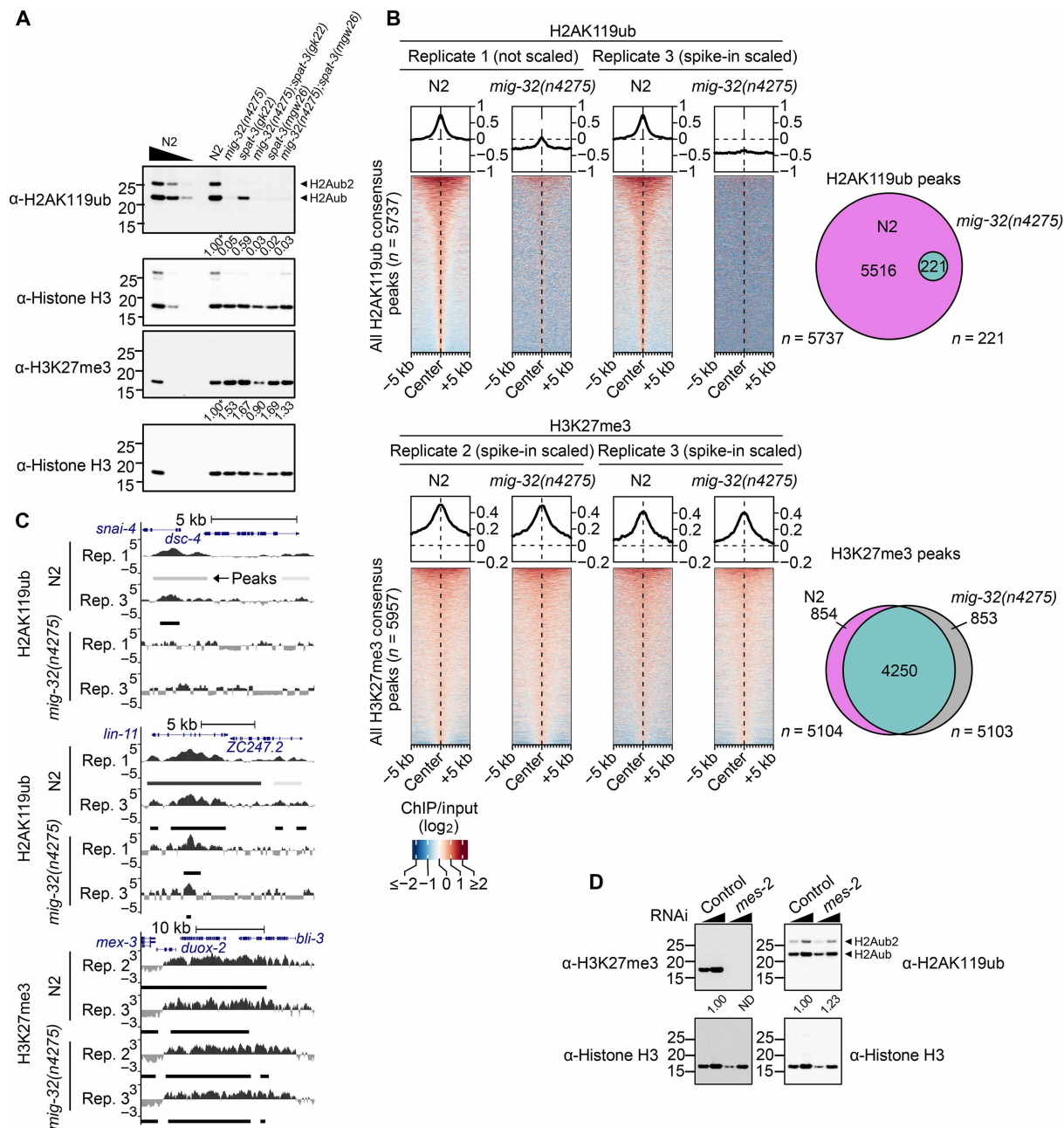
Fig. 3. Accumulation of H2AK119ub and H3K27me3 is not interdependent in *C. elegans* embryos. (**A**) Western blot for H2AK119ub and H3K27me3 in *mig-32* and *spat-3* single and double mutants. Histone H3 was probed as a control. H2AK119ub, but not H3K27me3, is depleted in the mutants. The predicted relative migration distances are 23 kDa for H2AK119ub (H2Aub1), 31.6 kDa for H2Aub2, and 15 kDa for histone H3 and H3K27me3. See fig. S7 and table S1 for allele details. ND, not detectable. Quantification relative to N2 (*). (**B**) Heatmaps of H2AK119ub (top) or H3K27me3 (bottom) at the consensus peaks called in N2 (wild-type) and/or *mig-32(n4275)* deletion mutants (log$_2$-transformed ChIP/input ratios). Consensus peaks are those called in at least two biological replicates (based on replicates 1 to 4 for H2AK119ub and 1 to 3 for H3K27me3). Quantification of the number of peaks called in N2 versus *mig-32(n4275)* mutants is shown on the right. Most H2AK119ub, but not H3K27me3, is lost in the mutants. Replicate 2 and 3 are scaled by spike-in chromatin. All *mig-32(n4275)* H2AK119ub consensus peaks overlap those detected in N2. (**C**) UCSC Genome Browser view of a representative H2AK119ub peak that is lost in the *mig-32(n4275)* mutants (top), an H2AK119ub peak that is attenuated in the *mig-32(n4275)* mutants (middle), and an H3K27me3 peak that is retained in both genotypes (bottom). Coverage is displayed as the log$_2$-transformed ChIP/input ratio. Positions of model-based analysis of ChIP-Seq (MACS)2-predicted peaks are shown below with darker colors indicating higher −log$_{10}$(q value). Rep., replicate. (**D**) Western blot for H2AK119ub and H3K27me3 in embryos collected from adults exposed to control or *mes-2* RNA interference (RNAi). Histone H3 was probed as a control. H3K27me3, but not H2AK119ub, is depleted in the *mes-2* knockdown embryos. Quantification relative to N2.
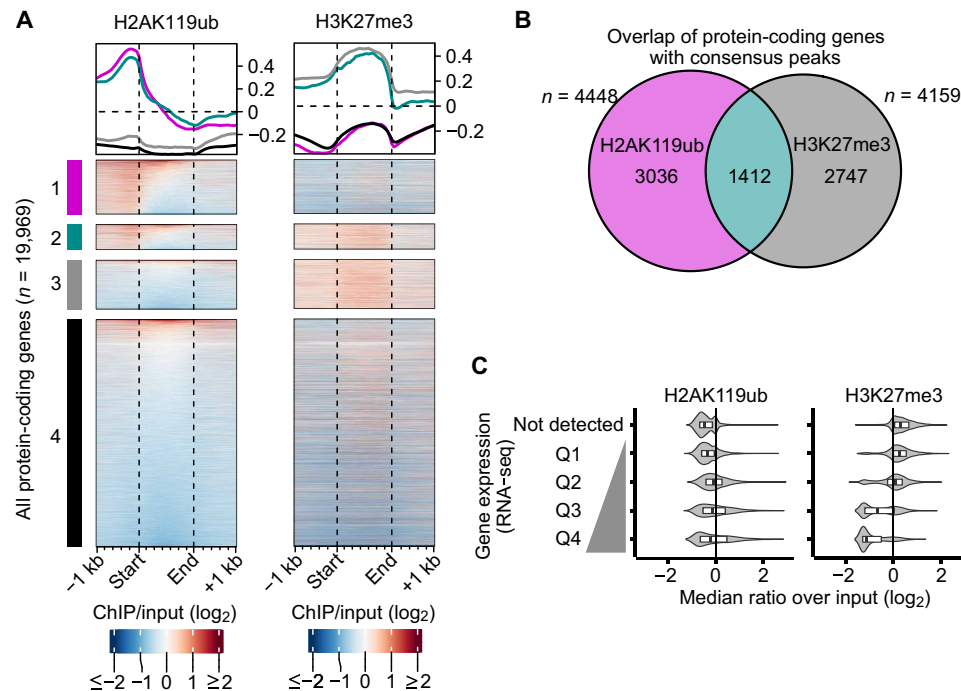
Fig. 4. H2AK119ub and H3K27me3 are enriched at different protein-coding genes. (**A**) Heatmaps of H2AK119ub and H3K27me3 ChIP-seq (log$_2$-transformed ChIP/input ratios) at all *C. elegans* protein-coding genes and flanking regions. The protein-coding genes are divided into four clusters, depending on their annotation with associated N2 consensus peaks: cluster 1: H2AK119ub only, cluster 2: both H2AK119ub and H3K27me3, cluster 3: H3K27me3 only, and cluster 4: neither an H2AK119ub nor an H3K27me3 peak. (**B**) Quantification of the overlap between genes associated with H2AK119ub and/or H3K27me3 from clusters 1 to 3 in (A). (**C**) Violin plots of the median H2AK119ub or H3K27me3 signal (log$_2$-transformed ChIP/input ratio) at the promoters of protein-coding genes divided into quartiles of expression based on RNA sequencing (RNA-seq) data in N2 (wild-type) embryos. H3K27me3, but not H2AK119ub, is enriched over promoters of silent or lowly expressed genes.

We further compared H3K27me3 and H2AK119ub-associated gene sets by examining their chromosomal locations and category of expression pattern (fig. S10) based on previously defined groups (*67*). Genes with H2AK119ub peaks, H3K27me3 peaks, or both H2AK119ub and H3K27me3 peaks are enriched in the "soma-specific" gene expression category and on the X chromosome, whereas they are depleted from the "germline-enriched" expression category (fig. S10). In contrast, genes uniquely associated with H2AK119ub, but not H3K27me3, peaks are enriched in the "ubiquitous" expression category (fig. S10). These patterns are consistent with the enrichment of H2AK119ub on the X chromosome (Fig. 1C and fig. S3) and the previously reported depletion of germline-expressed genes from the X chromosome (*37*). Furthermore, enrichment at broadly expressed genes supports roles for H2AK119ub in addition to gene repression.

H2AK119ub at genes encoding regulators of neuronal development and function

To gain insight into the biological functions regulated by H2AK119ub and/or H3K27me3, we performed GO enrichment analysis. The network of enriched terms, with clusters annotated by the term with best-ranked interconnectivity (*68*), reveals the common and distinct functional associations of genes marked by one or both modifications (Fig. 5A and table S4A). For H2AK119ub, the most prominent cluster is annotated with the term "cell morphogenesis involved in neuron differentiation" and is connected to clusters representing neurotransmitter secretion and negative regulation of cell communication (Fig. 5A). This enrichment is consistent with roles of *mig-32* and *spat-3* in neuronal migration, axon guidance, and neuronal cell

fate (*31–33*). Genes with H3K27me3 or both H2AK119ub and H3K-27me3 peaks also show enrichment for GO terms related to the nervous system, including neuron development and synaptic signaling (Fig. 5A). Notably, H2AK119ub/H3K27me3 coenriched genes are also uniquely associated with male anatomical structure morphogenesis (table S4A), which is consistent with defects in sensory ray development of the male tail observed in mutants for both *C. elegans* PRC1 and PRC2 subunit homologs (*31, 35*). Overall, the GO enrichment map reflects the known somatic functions of *C. elegans* Polycomb complexes and is a resource to prioritize candidate genes and identify the genetic networks underlying these phenotypes.

Considering the known axon guidance phenotypes in *mig-32* and *spat-3* mutants and the enrichment of GO terms related to neuron development at H2AK119ub-marked genes, we examined a curated list of genes known to be involved in axon guidance (*69*). Notably, 74% of these genes are associated with H2AK119ub peaks (61/82; $P < 2.2 \times 10^{-16}$, Fisher's exact test; Fig. 5B). Axon guidance genes encode intracellular, extracellular, and cell surface factors (*69*), and there is a high overlap with H2AK119ub peaks for all categories (61 to 86%; Fig. 5C). In addition, genes with H2AK119ub peaks include components of four major conserved axon guidance pathways—netrin (e.g., *unc-6*/netrin secreted cue; Fig. 5D), Slit/Robo (e.g., *sax-3*, a major Slit receptor; Fig. 5D), Ephrin, and Semaphorin signaling (*69*). A subset of these genes is also misregulated in PRC1 mutants (see below) and represents key candidates underlying the axon guidance phenotypes in PRC1 mutants (*31, 32*). Furthermore, these data suggest that PRC1/H2AK119ub may act through both cell-autonomous and nonautonomous mechanisms to regulate axon guidance.
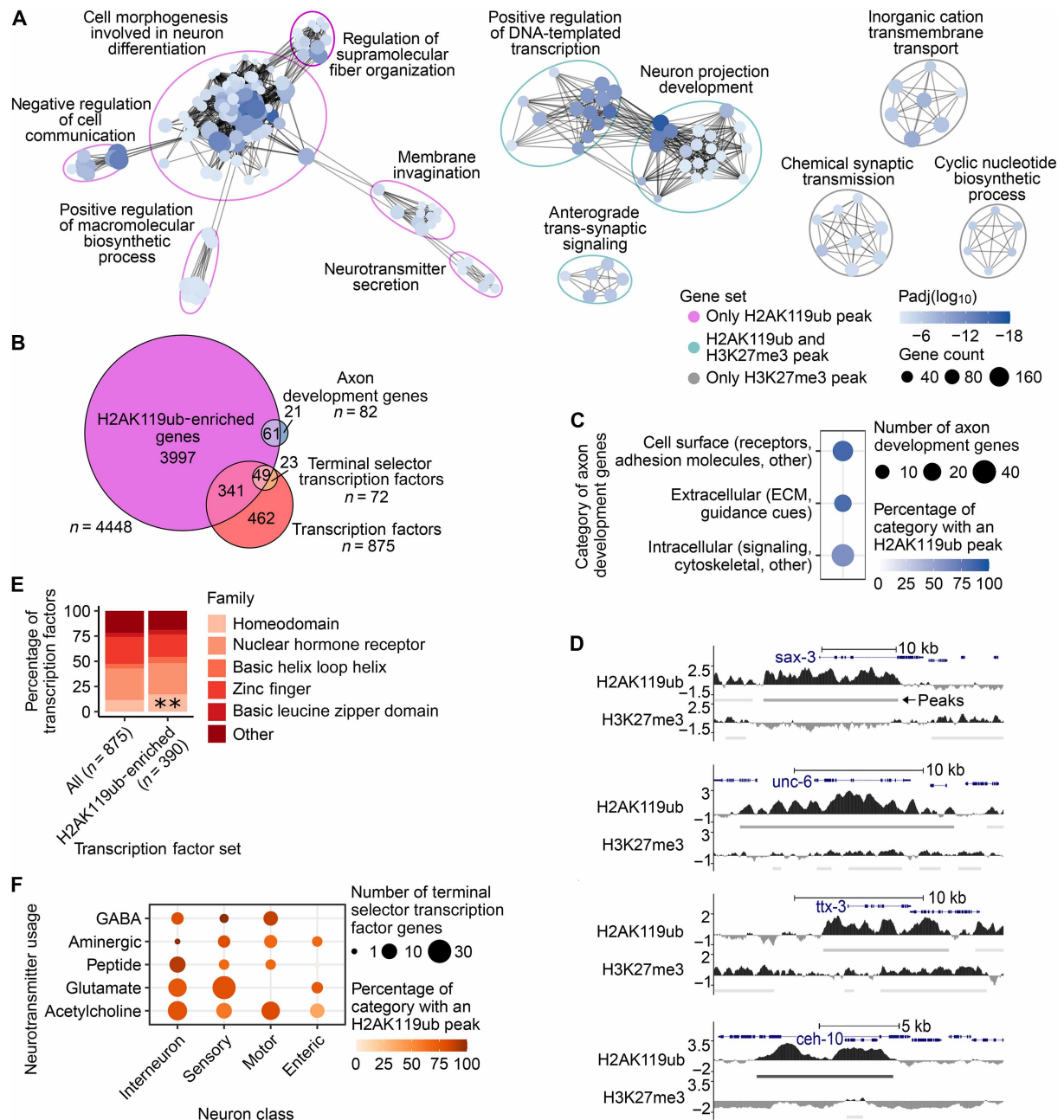
Fig. 5. Genes with H2AK119ub peaks are enriched for neuronal functions. (**A**) Enrichment map of GO terms overrepresented among genes with H2AK119ub (149 terms), H3K27me3 (21 terms), or both H2AK119ub and H3K27me3 N2 consensus peaks (41 terms, including 34 that overlap with H2AK119ub- and H3K27me3-only sets). See table S4 and Materials and Methods for details. Node size indicates the number of genes associated with the term, and edges indicate overlap of gene sets. (**B**) Significant overlap of H2AK119ub-associated genes with transcription factors (*71*), terminal selector transcription factors (*72*), and genes involved in axon guidance (*69*). $P < 2.2 \times 10^{-16}$; Fisher's exact test. (**C**) For three categories of axon guidance factors (*69*), the dot plot shows the number of genes per category and the percentage of the category associated with an H2AK119ub peak. ECM, extracellular matrix. (**D**) UCSC Genome Browser view of H2AK119ub and H3K27me3 enrichment and peaks at representative axon guidance (*69*) (top, *sax-3*, and *unc-6*) and terminal selector transcription factor (bottom; *ttx-3* and *ceh-10*) genes. Positions of MACS2-predicted peaks are shown below with darker colors, indicating higher $-\log_{10}(q$ value). (**E**) Proportion of transcription factors in each family (*71*) genome wide or for genes with an H2AK119ub peak. Genes with H2AK119ub peaks are enriched for homeodomain transcription factors (** indicates significant enrichment, $P = 3.6 \times 10^{-6}$; Fisher's exact test). (**F**) Dot plot of the number of terminal selector transcription factors (*72*) associated with each major neuron class, separated by neurotransmitter use. The percentage of each gene set with an H2AK119ub peak is shown by the color. Some terminal selectors are associated with multiple neuron types. GABA, γ-aminobutyric acid.

The genes with H2AK119ub and H3K27me3 peaks are enriched for GO terms related to positive regulation of DNA-templated transcription, a parent term of DNA binding transcription factor activity (70). To directly assess the enrichment of H2AK119ub at transcription factor genes, we examined a list of all known transcription factor genes (71) and found a significant overlap with genes that have H2AK119ub peaks (45%, 390/875; $P < 2.2 \times 10^{-16}$, Fisher's exact test; Fig. 5B). Furthermore, transcription factors with H2AK119ub peaks are 2.8-fold more likely to contain a homeodomain compared to all transcription factors ($P = 3.6 \times 10^{-6}$; Fisher's exact test) (Fig. 5E). Homeodomains are overrepresented among transcription factors known as "terminal selectors," which are required for neuron type–specific terminal differentiation (72). Among genes encoding the known terminal selector transcription factors (72), 68% (49/72, $P < 2.2 \times 10^{-16}$; Fisher's exact test) have H2AK119ub peaks (Fig. 5B). Moreover, the H2AK119ub-enriched terminal selector transcription factors are required to specify neurons of all major classes and neurotransmitter usage types (Fig. 5F). Notably, the H2AK119ub-enriched group includes two homeodomain terminal selectors, ttx-3 and ceh-10 (Fig. 5D, bottom), which specify the cell fate of the AIY cholinergic interneuron (33). PRC1 was previously found to be required cell autonomously for AIY fate and maintenance of ttx-3 and ceh-10 expression (33). Our data indicate that this regulation is likely through a direct H2AK119ub-dependent mechanism. Together, these data suggest that H2AK119ub influences neuronal development by regulating axon guidance signaling pathways and neuronal identity via terminal selector transcription factor expression.

Genes misregulated in H2AK119ub-deficient mutants are enriched for nervous system functions

To investigate the role of H2AK119ub in the regulation of gene expression, we performed RNA-seq in N2 (wild-type), mig-32(n4275), spat-3(mgw26), and mig-32(n4275);spat-3(mgw26) late embryos (Fig. 6, fig. S11, and tables S2 and S3). The highest magnitude changes corresponded to increased expression in the PRC1 mutants (81 to 94% of genes with at least a twofold change; Fig. 6A). However, genes with more modest but statistically significant changes (1.5-fold change, adjusted $P \le 0.05$) show up-regulation (40 to 70%) and down-regulation (30 to 60%) in similar proportions (Fig. 6A). The latter cutoff is used in the analyses below, in particular because these modest changes may reflect differences in specific cell types that are partially masked when examining the embryos as a whole. Moreover, this cutoff has been used previously to identify genes differentially expressed following manipulation of Polycomb complexes (14, 73).

The gene expression changes are highly concordant overall across the PRC1 mutant genotypes (Fig. 6B and fig. S11B). The genes with increased expression in PRC1 mutants are largely shared between spat-3(mgw26) and mig-32(n4275);spat-3(mgw26) genotypes (60%, 350/582; fig. S12A) and are enriched for neuronal functions including regulation of trans-synaptic signaling and neurotransmitter transport (fig. S12B and table S4B). The genes with decreased expression in PRC1 mutants are detected as differentially expressed at a higher frequency in the mig-32(n4275);spat-3(mgw26) double mutants than in the single mutants (fig. S12A). However, these genes do show similar down-regulation trends in both the mig-32 and spat-3 single mutants (Fig. 6B). Notably, while fewer differentially expressed genes were detected in mig-32(n4275) mutants (Fig. 6A and fig. S12A), these genes are highly overlapping with the other mutants (58/59 up-regulated and 58/70 down-regulated; fig. S12A). Although one

possibility is that spat-3 plays a more prominent role than mig-32 in regulation, we favor the interpretation that small differences in embryo staging and the inherent heterogeneity of the samples accounts for a decreased power to detect significant differences in the mig-32 mutants. The overall similarity of gene expression changes among the three PRC1 mutant genotypes (Fig. 6B and fig. S11, B and C) supports mig-32 and spat-3 predominantly working in concert.

To determine how the genes differentially expressed in PRC1 mutants correlate with Polycomb modifications, we clustered them based on proximal H2AK119ub and H3K27me3 patterns and expression differences (Fig. 6C) and determined their overlap with H2AK119ub and H3K27me3 peaks (Fig. 6D) and GO term enrichment (Fig. 6E and table S4C). Clustering analysis subsets genes with high H2AK119ub enrichment and both increased (47%) and decreased (53%) expression (cluster 1) and genes with weaker upstream H2AK119ub along with gene-body H3K27me3 (cluster 2), most of which show increased expression in mutants (81%, 474/583) (Fig. 6C). As seen for peaks (Fig. 3), H2AK119ub is reduced in mig-32 mutants for genes in both cluster 1 and cluster 2. However, the H3K27me3 enrichment on genes in cluster 2 is not significantly different in mig-32 mutants (Fig. 6C and fig. S12C). Notably, the subset of differentially expressed genes enriched for both H2AK119ub and H3K27me3 (Fig. 6, C, cluster 2, and D) supports potential cooperation between H2AK119ub and H3K27me3 at these targets, which may be revealed by combinatorial depletion of PRC1 and PRC2.

Both cluster 1 and cluster 2 reveal strong candidate genes that may contribute to neuronal defects in mig-32 and spat-3 mutants (31–33), including transcription factors and neuron development genes (e.g., hlh-14, hlh-16, and ngn-1; cluster 1), and known axon guidance genes (69) (e.g., cdh-4, cluster 1, aex-3, unc-52, and rpm-1; cluster 2) (Fig. 6, C and E). Furthermore, GO analysis reveals significant enrichment of terms including neuron differentiation, trans-synaptic signaling, and neurotransmitter transport in these clusters (Fig. 6E). Differentially expressed genes lacking H2AK119ub or H3K27me3 enrichment (Fig. 6, C, cluster 3, and D) mostly show decreased expression in PRC1 mutants. These genes may be regulated in an indirect manner, through H2AK119ub-independent activity, or may be H2AK119ub modified in specific or rare cell types, and thus, H2AK119ub enrichment is masked when profiling whole embryos.

Many of the H2AK119ub-enriched genes are not detectably differentially expressed upon loss of this histone modification in mig-32 and/or spat-3 mutants (Fig. 6D). The H2AK119ub/H3K27me3-marked subset may be regulated redundantly by the PRC1-like and PRC2 complexes, as has been reported in mammals (13), and/or H2AK119ub may be otherwise dispensable for regulation of these genes. Alternatively, these genes may show cell type–specific expression changes that are masked in analysis of whole embryo transcriptomes. For the H2AK119ub-enriched gene encoding terminal selector transcription factor TTX-3 (Fig. 5D), previous single-molecule RNA–fluorescence in situ hybridization (33) found that ttx-3 mRNA was reduced in the mother cell of the AIY neuron in mig-32 and spat-3 mutants. However, while there is a down-regulation trend in all three PRC1 mutant genotypes, ttx-3 is not called as significantly differentially expressed by our criteria (table S3) (13). Overall, together with the enrichment of H2AK119ub at genes with neuronal functions (Fig. 5A), the transcriptome analysis supports a conserved role for PRC1 in the regulation of neuronal gene expression (Fig. 6E) (23, 24, 26–28) and both H3K27me3-dependent and H3K27me3-independent activities of the PRC1-like complex in C. elegans.
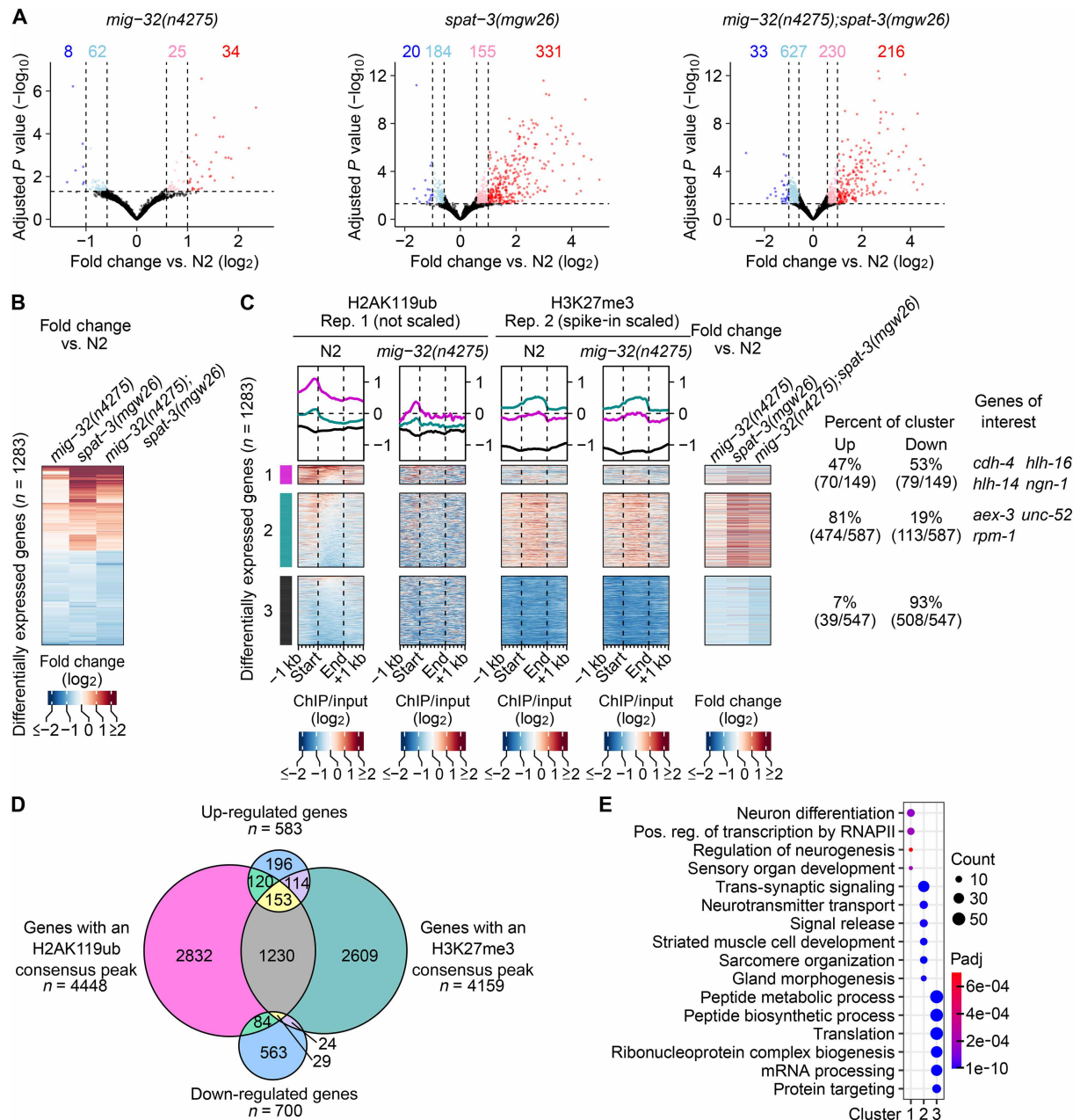
Fig. 6. Differential gene expression in H2AK119ub-deficient mutants. (A) Volcano plots of RNA-seq data in *mig-32(n4275)*, *spat-3(mgw26)*, and *mig-32(n4275);spat-3(mgw26)* mutants. Significantly differentially expressed genes (*P* adjust ≤ 0.05) with an absolute fold change of at least 2 (log₂ fold change of 1) are marked in red (up-regulated) or blue (down-regulated). Significantly differentially expressed genes with an absolute fold change of at least 1.5 (absolute log₂ fold change of 0.58) are marked in pink (up-regulated) or light blue (down-regulated). (**B**) Fold change in each mutant genotype compared to wild type (N2) for the differentially expressed genes detected in any of the three comparisons in (A). (**C**) Heatmaps of H2AK119ub and H3K27me3 (log₂-transformed ChIP/input ratios) at the differentially expressed protein-coding genes. Fold change (log₂) in each mutant genotype is displayed. The differentially expressed genes are grouped into three *k*-means clusters based on H2AK119ub and H3K27me3 enrichment and fold change. (**D**) Quantification of the overlap of protein-coding genes annotated with H2AK119ub N2 consensus peaks, H3K27me3 N2 consensus peaks, or called as significantly up- or down-regulated in H2AK119ub-deficient mutants. (**E**) Enriched GO biological process terms associated with the differentially expressed protein-coding genes in each of the *k*-means clusters in (C). Pos. reg., positive regulation.

Repressed enhancers are H2AK119ub enriched in embryos

As described above, H2AK119ub is highly correlated with H3K4me1 and enriched at enhancer-associated chromatin states (Figs. 1D and 2 and fig. S5). To determine how H2AK119ub affects enhancer-mediated gene regulation, we assigned the predicted active or repressed enhancers (*56*) to the nearest gene and examined their association with

H2AK119ub (Fig. 7 and fig. S13A). The active or repressed enhancer states correspond to enhancers with H3K27ac or weak H3K27me3 enrichment, respectively (*56*). When genes differentially expressed in H2AK119ub-deficient embryos are clustered by the presence of these enhancers, H2AK119ub and the enhancer-associated H3K4me1 and/or H3K27ac are coenriched at the enhancer positions, and genes with
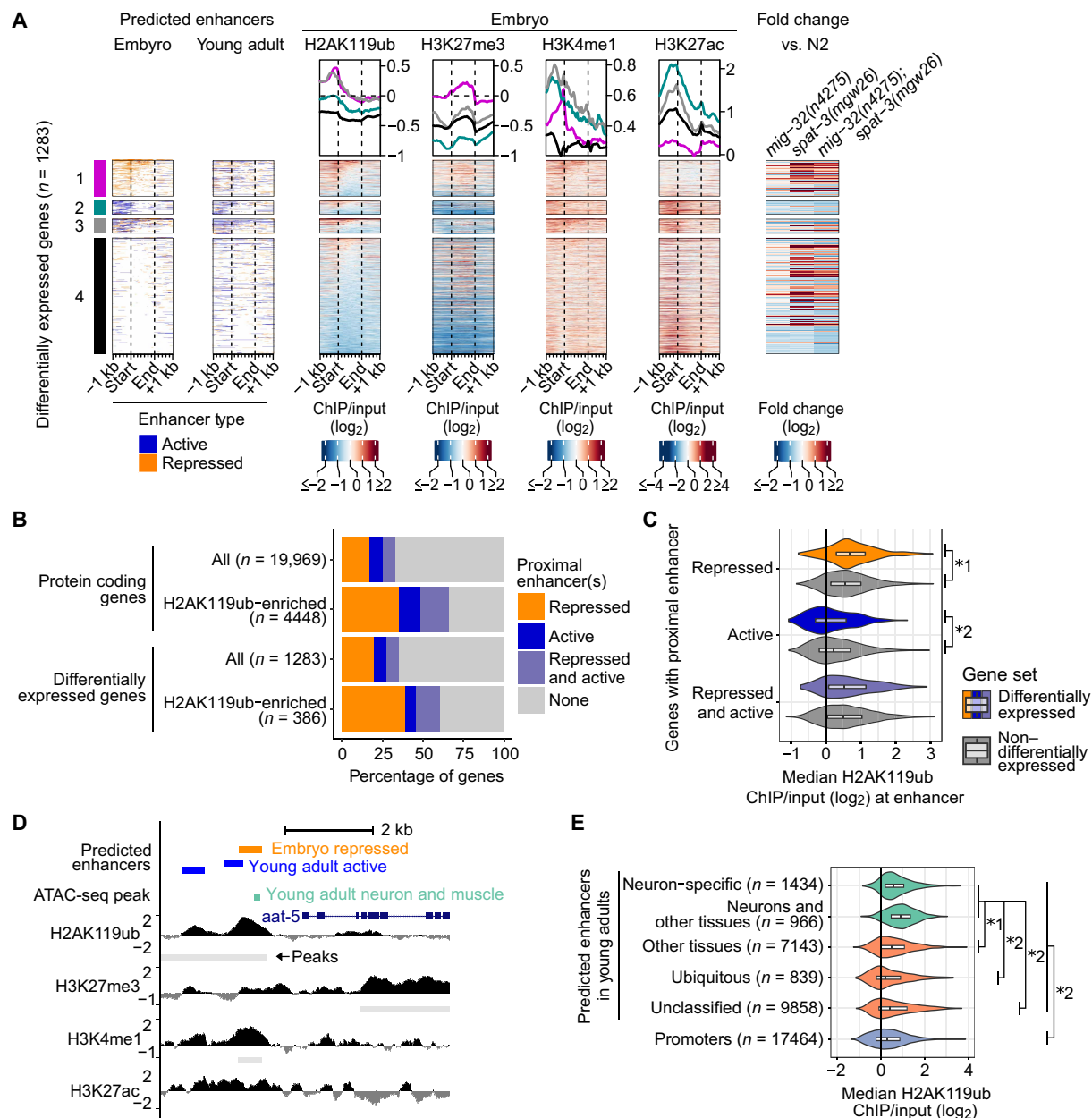
Fig. 7. H2AK119ub is enriched at predicted enhancers with developmentally dynamic expression. (**A**) Heatmaps of predicted enhancer positions (*56*), H2AK119ub, H3K27me3, H34K4me1, and H3K27ac (log₂-transformed ChIP/input ratios) at all differentially expressed genes and their flanking regions. Genes are grouped into four clusters, depending on their annotation with a predicted enhancer region(s): cluster 1: repressed enhancers, cluster 2: active enhancers, cluster 3: both repressed and active enhancers, and cluster 4: no enhancer. (**B**) Quantification of the proportion of all protein-coding genes, protein-coding genes associated with an H2AK119ub N2 consensus peak, all differentially expressed genes, or differentially expressed genes associated with an H2AK119ub N2 consensus peak annotated with the indicated type of proximal predicted enhancer. (**C**) Median H2AK119ub signal (log₂-transformed ChIP/input ratios) at predicted enhancers associated with differentially expressed genes and nondifferentially expressed genes. *1, $P = 4.1 \times 10^{-5}$ and *2, $P = 8.9 \times 10^{-3}$; Mann-Whitney U test. (**D**) UCSC Genome Browser view of a representative genomic region with predicted enhancer regions (*56*), assay for transposase-accessible chromatin (ATAC)-seq peak (*58*), ChIP enrichment, and MACS2-predicted peaks for H2AK119ub, H3K27me3, H3K4me1, and H3K27ac. (**E**) Violin plot of median H2AK119ub (log₂-transformed ChIP/input ratios) in embryos at predicted enhancers and promoters that are accessible in young adults (*48, 58*). Predicted enhancers are grouped on the basis of their accessibility patterns in the profiled young adult tissues (*58*). Unclassified enhancers have weak accessibility (*58*). *1, $P = 2.9 \times 10^{-8}$ and *2, $P < 2.2 \times 10^{-16}$; Mann-Whitney U test.

proximal enhancers have higher associated levels of H2AK119ub (Fig. 7A, clusters 1 to 3 versus cluster 4). A similar pattern is also seen across all protein-coding genes (fig. S13A). Furthermore, the proportion of all genes and of differentially expressed genes that are associated with proximal enhancers is significantly higher for the subset that are also associated with H2AK119ub peaks (Fig. 7B; 66% versus 33% and 61% versus 35%; $P < 2.2 \times 10^{-16}$, Fisher's exact test). These H2AK119ub peaks overlap with the enhancer in nearly all cases (93%) (Fig. 7A and fig. S13A). This high enrichment of proximal enhancers at H2AK119ub-associated genes is consistently observed with a different set of enhancer predictions (fig. S13, B and C) (57) and suggests that H2AK119ub-dependent misregulation of enhancer activity is at least partially responsible for the gene expression changes in *mig-32* and *spat-3* mutants.

We next compared H2AK119ub enrichment and H2AK119ub-dependent gene expression changes associated with repressed versus active enhancers. Among the differentially expressed genes, the H2AK119ub-enriched subset is 1.9-fold more likely to be associated with a repressed enhancer (Fig. 7B). The differentially expressed genes with an H2AK119ub-overlapping repressed enhancer are mostly up-regulated in *mig-32* and *spat-3* mutants (72%; 108/150). The repressed enhancers proximal to differentially expressed genes are also more highly enriched for H2AK119ub than those proximal to non–differentially expressed genes ($P = 4.1 \times 10^{-5}$; Mann-Whitney U test) (Fig. 7, A and C). For example, upstream of a representative gene, *aat-5*, is co-occurring peaks of H2AK119ub and H3K4me1 that overlap with a predicted enhancer that is repressed in embryos (Fig. 7D) (56). In *mig-32(n4275)* mutants, this H2AK119ub peak is lost, and the putative target gene, *aat-5*, is up-regulated in H2AK119ub-deficient animals. In contrast, the active enhancers that are associated with differentially expressed genes have on average less H2AK119ub enrichment than those associated with non–differentially expressed genes ($P = 8.9 \times 10^{-3}$; Mann-Whitney U test), and the majority of the proximal genes (76%, 72/95) are down-regulated in the *mig-32* and *spat-3* mutants (Fig. 7, A and C). Collectively, these results suggest that the PRC1-like complex regulates enhancer activity, with a more prominent role for H2AK119ub in constraining the activity of repressed enhancers during embryonic development.

Embryonic H2AK119ub is enriched at neuronal enhancers

To investigate the temporal and tissue-specific dynamics of H2AK119ub-enriched enhancers, we examined the developmental stages and cell types in which these enhancers become accessible in a wild-type context. To assess their activity across developmental stages, we examined predicted repressed and active enhancer positions in young adults (Fig. 7A and fig. S14A). We find a general pattern of accumulation of active enhancers proximal to genes in young adults, including proximal to those with only repressed enhancers in embryos. This pattern suggests that these H2AK119ub-enriched regions become more accessible later in development, potentially allowing for enhancer-mediated expression of their target genes. To determine tissue-specific activity, we looked at the enrichment of H2AK119ub in embryos at promoters, as well as at enhancers that are divided into categories based on their accessibility in different tissues in young adults (48, 58) (Fig. 7E and fig. S14B). Embryonic H2AK119ub is most highly enriched at enhancers that are accessible in neurons, when compared to those accessible in nonneuronal or all tissues ($P = 2.9 \times 10^{-8}$ and $P < 2.2 \times 10^{-16}$; Mann-Whitney U

test) (Fig. 7, D and E, and fig. S14B). Furthermore, the enrichment of H2AK119ub at every enhancer category is significantly higher than at promoters ($P < 2.2 \times 10^{-16}$; Mann-Whitney U test) (Fig. 7E), suggesting that H2AK119ub has a larger influence on enhancer as opposed to promoter activity. Together, these findings support a role for H2AK119ub in developmental stage–specific regulation of neuronal enhancer activity in *C. elegans*.

DISCUSSION
Probing the functions of Polycomb complexes in diverse organisms and contexts provides valuable insight into the conservation of their mechanisms and roles in development. Using *C. elegans* embryos as a model, we uncovered a genome-wide enrichment of H2AK119ub at enhancer regions, which show developmentally dynamic accessibility, particularly in neuronal tissue. The identification of gene networks regulated by H2AK119ub in *C. elegans* expands the repertoire of neuronal functions regulated by PRC1 and underscores its conserved importance in neuronal gene regulation (23, 30). Our findings provide evidence for both cooperative and independent functions of PRC1 and PRC2 and challenge the conservation of established interdependent recruitment models. Furthermore, our study supports both the well-characterized role of PRC1 at H3K27me3-repressed chromatin, as well as an expanded role in the modulation of enhancer activity.

Relationships between PRC1/H2AK119ub and PRC2/H3K27me3
The evolutionary conservation of H2AK119ub and H3K27me3 interdependence is an active area of investigation. Our finding that H3K27me3 levels and peak patterns are maintained upon disruption of H2AK119ub in *C. elegans* stands in contrast to the highly interdependent levels of these marks in other systems, with the caveat that our study only investigates one time point in development. In the interdependent recruitment model, PRC1 complexes are recruited to sites of H3K27me3, and PRC2 complexes are recruited to sites of H2AK119ub by subunits that can recognize and bind each mark (1, 74–76). Therefore, loss of either histone modification can impede recruitment and accumulation of both complexes, as well as their corresponding histone modifications, at target regions (41, 42). Disruption of PRC1 results in a global reduction of H3K27me3 enrichment and PRC2 component binding in mouse embryonic stem cells, early zebrafish embryos, and *Drosophila* embryos (10, 11, 41, 42, 62). Similarly, loss of vPRC1 or PRC2 components leads to depletion of both H2AK119ub and H3K27me3 at a subset of Polycomb targets, including the inactive X chromosome, in mouse embryoid bodies and embryonic fibroblasts (15, 77, 78). In addition, maternal depletion of either Polycomb complex disrupts both histone modifications at maternal imprinting sites in early mouse embryos (79, 80). Notably, homologs for H2AK119ub-binding PRC2 subunits have not been identified in *C. elegans* (81), and it is not known whether H3K27me3-binding proteins (82) associate with PRC1. Together with our finding that these marks are largely not interdependent, one possibility is that *C. elegans* has evolved a distinct mechanism to regulate the levels and distribution of H2AK119ub and H3K27me3 that does not depend on the presence of the other complex or detection of the other histone modification. This model is in line with recent evolutionary evidence that vPRC1 predates cPRC1 and that PRC1 cross-talk with PRC2 emerged later (83).

The RING1/PCGF heterodimer is the core of both canonical and vPRC1 complexes. However, in mouse, human, *Drosophila*, and zebrafish, multiple PCGF proteins each define a distinct PRC1 complex with a unique combination of accessory subunits, associated activities, and varying relationships with PRC2 (*3, 81, 84*). To date, SPAT-3 and MIG-32 are the only RING1 and PCGF homologs, respectively, identified in *C. elegans* (*31, 81*), and it is unclear whether multiple distinct *C. elegans* PRC1-like complexes exist. In addition, while we and others (*31*) have shown that loss of MIG-32 leads to loss of bulk H2AK119ub, MIG-32 can also mediate compaction of nucleosome arrays in vitro (*85*), which suggests a cPRC1-like and potentially H2AK119ub-independent mechanism of gene repression. This cPRC1-like activity may act redundantly with PRC2 and H3K27me3 (*13, 86*). While we identified mostly distinct gene sets associated with H2AK119ub and H3K27me3, our data are also consistent with redundant regulation at a subset of genes. These candidates are the genes coenriched with both marks and for which expression changes were not detected in *mig-32* or *spat-3* mutants. These findings would be consistent with PRC1 and PRC2 acting in parallel to repress lineage-specific genes and transcription factors in mammals (*13, 84, 86*). Overall, our work has revealed distinct and conserved aspects of *C. elegans* Polycomb regulation. Further work, including identification of the PRC1-like and PRC2-interacting proteins and combinatorial depletion of PRC1 and PRC2, will be required to fully elucidate the gene regulatory and targeting mechanism of these complexes.

A role for H2AK119ub on the X chromosome

Chromatin-based mechanisms play conserved roles in regulating sex chromosomes across species. Here, we find an enrichment of H2AK119ub coverage across the X chromosome and H2AK119ub peaks at X-linked genes, thus implicating the *C. elegans* PRC1-like complex in dosage compensation. In *C. elegans* hermaphrodites, the two X chromosomes are repressed by PRC2 and H3K27me3 in the germline and by the DCC and H4K20me1 in the soma (*87*). Because H2AK119ub and H3K27me3 are coenriched on the X, this chromosome may contain genomic locations that are regulated by the two marks cooperatively in the germline. The utilization of both histone modifications for repression on a chromosome-wide scale would be consistent with the importance of both PRC1 and PRC2 in mammalian X inactivation (*88*), although the specific mechanisms of X-chromosome silencing are distinct between mammals and *C. elegans*. Alternatively, H2AK119ub may be enriched on the X chromosome in somatic cells by the DCC. H2AK119ub could potentially function in a similar manner to, or along with, H4K20me1, which is a downstream effector of DCC binding that leads to X-linked gene silencing via chromatin compaction (*49, 51, 52*).

A conserved role for H2AK119ub at enhancers

One of the most notable findings of our analysis was the enrichment of H2AK119ub at predicted enhancer regions rather than facultative heterochromatin or repressed states. These enhancers were computationally predicted by histone modification signatures and further supported by whole-animal and tissue-specific assay for transposase-accessible chromatin (ATAC)-seq, as well as experimental validation of candidates (*48, 56–58*). We speculate that H2AK119ub and PRC1 may have multiple developmental stage–specific roles in enhancer-driven gene expression. The first and more abundant class of H2AK119ub-enriched enhancers we detected are not predicted to be active in embryos but generally gain active enhancer chromatin signatures and increased accessibility later during development. The subset of differentially expressed genes proximal to these enhancers tends to be up-regulated in the H2AK119ub-deficient mutants, suggesting that PRC1 constrains their activity and loss of H2AK119ub allows acquisition of an active state. The second class, which showed relatively less H2AK119ub enrichment, is predicted to be active H3K4me1/H3K27ac-enriched enhancers in embryos. The genes proximal to these enhancers that were differentially expressed were generally down-regulated in the *mig-32* and *spat-3* mutants, which suggests that PRC1 promotes their enhancer-mediated expression but in a manner that is temporally uncoupled from or less dependent on H2AK119ub deposition. Collectively, these findings lead to a model of H2AK119ub as part of a "poised" or "primed" enhancer state to prevent precocious or inappropriate enhancer activation and/or to facilitate timely gene induction (*89*). While the precise mechanisms remain to be determined, recent work in other systems points to the role of H2AK119ub in promoting accessibility in vitro (*18*) and of PRC1 in influencing three-dimensional chromatin configurations that can promote or repress gene expression, including in *Drosophila*, mouse NPCs, and cancer (*90*). Further studies examining interactions with transcription factors or the transcription machinery and effects on chromatin topology will reveal how *C. elegans* PRC1 may influence enhancer configuration and activity.

Control of neuronal gene expression by Polycomb repressive complexes

Our genome-wide analysis revealed a strong enrichment among both H2AK119ub-marked and PRC1-regulated genes for nervous system functions including neurogenesis, axon guidance, neuron differentiation, and trans-synaptic signaling. While previous work uncovered roles for *mig-32* and *spat-3* in migration, axon guidance, and cell fate in specific neurons (HSN, PVQ, and AIY) (*31–33*), the target genes identified in our work and, in particular, the widespread association of H2AK119ub with key transcription factors that regulate neuronal identity, suggest a more broad role for PRC1 in nervous system development than previously appreciated. A full understanding of this role will be facilitated by systematic analyses including single-cell approaches and tools available in *C. elegans* to assess cell fate of the entire nervous system (*91*). Dissecting the roles of PRC1 homologs in *C. elegans* nervous system development and function may also provide insight into the pathogenic mechanisms of H2AK119ub misregulation in neurodevelopmental syndromes (*30*).

To our knowledge, this work provides the first global snapshot of gene regulation by *C. elegans* PRC1; however, the analysis of whole embryos is a limitation that precludes determining whether the detected H2AK119ub and/or gene expression changes reflect the activity of PRC1 within the nervous system or in other cell types. Processes such as axon guidance are known to involve both cell-autonomous and nonautonomous gene regulation (*69, 92*). In addition, Polycomb complexes repress nonlineage differentiation programs in various cell types in mammals to ensure proper canalization of cell fate (*12, 93*), and it is therefore possible that PRC1-mediated repression of genes associated with neuronal development in nonneuronal tissues contributes to our findings. However, several lines of evidence support a substantial role for the activity of PRC1 within the nervous system in our data. First, approximately one-third of the cells in late embryos are neurons or neuronal precursors (*94*). Second, *mig-32* and *spat-3* function cell autonomously to regulate cell fate of the AIY interneuron

(*33*), and PRC1 regulates gene expression in neurons in other organisms (*23*). However, cell type–specific gene expression analysis is needed to fully address the role of PRC1 in neurons versus other cell types.

Even within the nervous system, PRC1 activity and cooperation with PRC2 can also be developmental stage specific. In neuronal stem and progenitor cells in other organisms, PRC1 functions together with PRC2 to maintain differentiation factors in a poised state (*24, 95–98*). In contrast, studies in differentiating and differentiated neurons in mice and *C. elegans* indicate that PRC1 acts independently of PRC2 to maintain transcriptional programs (*28, 33*). The H2AK119ub-enriched regions we identify show developmental stage–specific changes in their enhancer state and accessibility. As loss of PRC1 has variable effects on the expression of H2AK119ub-associated genes, and only a subset shows H3K27me3 coenrichment, our work contributes to the growing evidence that PRC1 has versatile and context-dependent roles in gene regulation and cooperation with PRC2, including in the nervous system (*24, 28, 33, 95–97*). A global investigation of the regulatory targets and requirements for PRC1 during *C. elegans* nervous system development will be integral to clarifying the functions of PRC1 during the specification versus maintenance of neuronal cell fate.

MATERIALS AND METHODS

Worm maintenance
Strains were maintained on nematode growth medium (NGM) agar with *Escherichia coli* OP50-1 as a food source as described (*99*) at 21°C unless specified otherwise. The N2 (Bristol) strain was used as wild type (*100*). Strains and alleles used are listed in table S1.

Synchronized worm growth
Embryos were isolated from gravid adults using standard alkaline hypochlorite treatment ("bleaching") as described (*99*). After three washes in M9 buffer supplemented with 0.01% (v/v) Triton X-100 (M9/Tx), embryos were allowed to develop to L1 diapause in M9/Tx buffer overnight with aeration. Synchronized populations were then grown as described below.

Chromatin immunoprecipitation
Animals arrested at L1 diapause were prepared by bleaching as described above. Arrested L1s were counted and seeded into 40 ml of S-Complete medium (*99*) with OP50-1 as a food source, at a final density of ~0.5 to 1.5 animals/μl. Animals were grown with aeration for 71 to 77 hours to gravid adulthood, and embryos were isolated again by bleaching. After washes with M9/Tx, embryos were processed for ChIP as described below either immediately or after a further 3 to 5 hours of growth with aeration.

ChIP was performed essentially as described (*101–103*) with minor modifications as follows. Embryos were collected by centrifugation (1000*g* for 3 min) and washed twice in phosphate-buffered saline (PBS) containing 0.01% (v/v) Tx (PBS/Tx). To cross-link, PBS/Tx was added to at least 80 times the pellet volume (PV), and 37% formaldehyde (Sigma-Aldrich, F8775) was added to a final concentration of 1.8%. Samples were incubated at room temperature with rotation for 25 min. Glycine was added to a final concentration of 125 mM, followed by incubation for an additional 5 min. All subsequent steps were performed on ice using prechilled buffers and tubes.

Embryos were washed twice with PBS/Tx as above, and an equal volume of resuspension buffer [50 mM Hepes-KOH (pH7.5), 150 mM NaCl, 1 mM EDTA, 0.01% Tx, and protease inhibitors (1 tablet per 5 ml; Roche, 4693159001)] was added to the embryo pellet. The resuspended embryos were aliquoted, snap frozen in liquid nitrogen, and stored at −80°C.

Aliquots of cross-linked embryos were thawed in an ice-water bath, the volume was adjusted to 3 to 4 PV using resuspension buffer, and 100 μl were aliquoted to each polystyrene sonication tube (Evergreen, 214-3721-010). An equal volume of resuspension buffer containing 2× detergents was added [50 mM Hepes-KOH (pH 7.5), 150 mM NaCl, 1 mM EDTA, 0.2% sodium deoxycholate, and 0.7% sodium sarkosyl]. Samples were sonicated in a Q800R3 water bath sonicator (QSonica, Q800R3-110; 50% power, 20-s on/20-s off) for 4 min. Samples were gently mixed by pipetting and sonicated for an additional 4 min.

The lysate was transferred to an Eppendorf tube, and an equal volume of resuspension buffer without detergents was added [50 mM Hepes-KOH (pH 7.5), 150 mM NaCl, and 1 mM EDTA]. The lysate was centrifuged (13,000*g* for 15 min at 4°C), and the supernatant was transferred to a new tube. Protein concentration was determined using the Bradford assay (Sigma-Aldrich, B6916). For samples including a spike-in control for calibration, sonicated *Drosophila* chromatin (Active Motif, 53083) was added at a ratio of 1:20 or 1:30 (table S2), where 1:20 is according to the manufacturer's recommendations for human samples but scaled down by the relative genome size of *C. elegans* versus human.

The supernatant was aliquoted to tubes for immunoprecipitation (IP), saving 15 to 20% of the volume of one IP tube as the "input" control, which was stored at −20°C. Tx (10%; v/v) was added to a final concentration of 1% (v/v). This step was omitted for anti-H3K27me3 (Cell Signaling Technology, 9733, C36B11), for which this detergent led to increased background (Saltzman; unpublished observations). See table S2 for antibody details. After antibody addition, samples were incubated overnight at 4°C with rotation. Protein G Dynabeads (Invitrogen, 10003D; 7.5 μl per IP) were prewashed twice with resuspension buffer and added to IPs, which were then incubated as above for 2 hours. Beads were collected on a magnetic stand (Permagen, MSR812) and washed as follows, with each wash incubated for 5 min at 4°C with rotation: 2× with FA-150 [50 mM Hepes-KOH (pH 7.5), 150 mM NaCl, 1 mM EDTA, 1% Tx, and 0.1% Sodium deoxycholate], 1× with FA-1M (FA-150 with 1 M NaCl), 1× with FA-0.5M (FA-150 with 0.5 M NaCl), 1× with TE-LiCl in a new tube [10 mM tris-Cl (pH 8), 1 mM EDTA, 250 mM LiCl, 1% IGEPAL CA-630, and 1% sodium deoxycholate], 2× with TE+ [10 mM tris-Cl (pH 8), 1 mM EDTA, 50 mM NaCl, and 0.005% IGEPAL CA-630].

Elution was performed in a new tube at 65°C for 15 min using 50 μl of ChIP elution buffer [10 mM tris-Cl (pH 8), 1 mM EDTA, 200 mM NaCl, and 1% SDS]. Elution was repeated, and the supernatants were pooled. The input aliquot was thawed and brought to 100 μl with ChIP elution buffer. Input and IP samples were treated with ribonuclease A (16.5 μg; Sigma-Aldrich, R4642) for 1 hour at 37°C and proteinase K (40 μg; Bioline, BIO-37084) for 2 hours at 55°C. Cross-links were reversed by incubation overnight at 65°C. DNA was isolated using a QIAquick PCR purification kit (QIAGEN, 28104). Input DNA was quantified using NanoDrop spectrophotometer or Qubit Fluorometer (Thermo Fisher Scientific).

ChIP-seq library preparation and ChIP-qPCR

Libraries were prepared with the NEBNext Ultra II DNA Library Prep Kit for Illumina (New England Biolabs , E7645S) according to the manufacturer's instructions using 25 to 50 ng of input DNA or half of ChIP DNA. Library concentration was quantified using NEB-Next Library Quant Kit for Illumina (NEB, E7630). Pooled libraries were sequenced using NextSeq500 or NestSeq2000 in 50– or 75– base pair (bp) paired-end mode. Details of read counts are in table S2.

For qPCR, input DNA samples were diluted 1:50, and ChIP samples were diluted 1:4. qPCR was performed with iTaq Universal SYBR Green Supermix (Bio-Rad, 1725121) in a 10-μl reaction. Primer efficiency was assessed by a fourfold dilution series of input DNA.

Analysis of *C. elegans* ChIP-seq data

The raw sequencing reads were trimmed for low-quality base calls, with a phred33 < 22, Illumina adapter sequences using a stringency of 12, and poly-G sequences (defined as 13 Gs in a row) using a stringency of 8 with TrimGalore v0.6.5 (104–106). The trimmed reads were then aligned to the *C. elegans* ce11 genome using Bowtie2 v2.3.4.3 (107) with the maximum fragment size parameter set to 2000. Alignments were filtered by removing duplicates and multimapping reads with a MAPping Quality (MAPQ) < 42, using Samtools v1.11 (108). Peaks were called with model-based analysis of ChIP-Seq (MACS)2 v2.2.7.1 (109) with -g option set to ce, -f option set to either BAMPE for paired-end libraries or BAM for single-end libraries, and the –broad option for all modifications except for H3K4me1, H3K4me3, and H3K27ac. Peaks that overlap with blacklisted regions, where there is artificially high signal, were removed (110). Replicates with a *Drosophila* chromatin spike-in were processed as above, except that they were aligned to a concatenated *C. elegans* ce11 and *Drosophila melanogaster* dm6 genome, reads mapped to both genomes were discarded, and the reads were normalized as described (10). Briefly, the ce11 reads were randomly subsampled using factors that reflect the total number of dm6 reads in that sample and were corrected for the ratio of dm6/ce11 reads in the corresponding input samples. Coverage files were prepared with the BEDTools v2.29.0 (111) genomecov function with the -bga option. For paired-end data, the -pc option was used. For single-end data, the -fs option was set as the fragment size predicted using SPP v1.15.4 (112). Log_2-transformed ChIP/input ratios were calculated per base with deepTools v3.5.0 bigwigCompare (113) with a pseudocount of 1.

Peaks of the same histone modification, including consensus peaks between replicates and peaks called in two genotypes, were defined as overlapping if at least 50% of the peak region overlapped with peak(s) in the two samples. The requirement for overlap could be satisfied by either peak. Briefly, for each pair of files compared, reciprocal overlapping peak sets were generated for each file using the BEDTools v2.29.0 (111) intersect function with the -f option set to 0.5 and the -e and -u option. Overlapping peaks were then determined from these two reciprocal overlapping peak sets by concatenating, coordinate sorting, and merging them using the BEDTools merge function with -c option set to 4, 5, and 6 (name, score, and strand BED fields) and -o option set to collapse, mean, and distinct. The nonoverlapping peaks for each of the two peak files were determined with the BEDTools intersect function with the -f option set to 0.5 and the -e and -v option included. Consensus peak sets were defined for N2 H2AK119ub and N2 H3K27me3 using replicates 0 and 1, corresponding to replicates A and B in Fig. 1, respectively. For analyses comparing N2 and *mig-32(n4275)* deletion mutants, consensus peak sets were defined using all replicates that included both genotypes: replicates 1 to 4 for H2AK119ub or replicates 1 to 3 for H3K27me3. References to N2 H2AK119ub and/or H3K27me3 consensus peak sets refer to the N2 consensus peak sets defined using replicate 0 (A) and 1 (B), unless otherwise indicated.

Peaks of two different histone modifications were defined as overlapping as follows. Briefly, for each pair of files compared, for each peak, the number of bases that overlap with peak(s) of the other histone modification was computed using BEDTools intersect with the option -wao. Overlapping peaks were then defined as those with a sum of overlapping bases that was at least 50% of their length, generating a list of overlapping peaks for each of the two modifications. To generate peak lists for heatmap plotting (e.g., Fig. 1A), these lists were concatenated, coordinate sorted, and merged using BEDTools as described above. The nonoverlapping peaks for each of the two original peak files were then determined with the BEDTools intersect function, comparing the original peak file and the set of overlapping peaks of interest, with the -v option included. To generate a stringent overlapping peak list with reciprocal 50% length overlap ("both" overlap), the two lists of overlapping peaks described above were intersected with BEDTools with the -u option and then concatenated, coordinate sorted, and merged. To generate a permissive overlapping peak list where the overlap can be satisfied by only one of the modification peaks ("either" overlap), each of the two lists of overlapping peaks described above and the peak file for the second modification were intersected with BEDTools with the -u option and then concatenated, coordinate sorted, and merged. Nonoverlapping peaks for each modification were then determined as described above.

Assigning ChIP-seq peaks and predicted enhancer regions to protein-coding genes

N2 consensus ChIP-seq peaks or predicted enhancer regions (56, 57) were assigned to the nearest gene in the WormBase WS263 release with ChIPseeker v1.28.3 (114) using the default genomicAnnotationPriority to prioritize assignment to a downstream gene and with the promoter region defined as within 500 bp of the gene start. Gene assignments were filtered for protein-coding genes (n = 20,094), and genes with no H2AK119ub or H3K27me3 ChIP or input signal across the entire gene body, 1 kb upstream or 1 kb downstream, were removed (n = 19,969). See table S3 for details of gene assignments.

Genomic data visualization

Matrices of ChIP-seq signals were produced with either the computeMatrix function of deepTools v3.5.0 (111) or the normalizeToMatrix function of EnrichedHeatmap v1.22.0 (115). For violin plots of H2AK119ub and H3K27me3 at gene promoters, computeMatrix was used with the –upstream option set to 500 and the –referencePoint set to the gene start site. For violin plots of H2AK119ub at chromatin states (56, 57) or predicted promoters and tissue-specific enhancers (58), computeMatrix was used with the -m option set to 1000 or 150, respectively. Before matrix computation, the enhancers regions (58) were merged using BEDTools merge with -c option set to 4 (BED name field) and -o option set to collapse. The same was done for each set of tissue-specific enhancers (58). For the chromosomal distribution heatmaps, computeMatrix was used with the –binsize set to 50,000. normalizeToMatrix was used for all other matrices of ChIP-seq signal with the window size set to 50 bp, background set

to 0, and the mean mode set to 0. The positions of the predicted enhancer regions (56–58) were visualized with matrices computed with normalizeToMatrix with the window size set to 50 bp, background set to 0, and the mean mode set to absolute. All heatmaps were made with the EnrichedHeatmap v1.22.0 (115) package, except for the heatmap of the Spearman correlation coefficients of histone modifications across all chromosomes. For this heatmap, correlation was computed using the base R function cor with method set to "spearman" and use set to "complete.obs," and the heatmap was plotted using Pheatmap v1.0.12 (116). Coverage tracks and peaks were visualized with the UCSC Genome Browser (117). Unless otherwise noted, $\log_2$-transformed ChIP/input coverage files from H2AK119ub replicate 1 and H3K27me3 replicate 1 were used for data visualization.

Mammalian ChIP-seq data
The fastq files for all mammalian ChIP-seq data were downloaded from Gene Expression Omnibus (GEO) (118). Details of GEO accession and sequence read archive (SRA) accession numbers can be found in table S2. The raw sequencing reads were trimmed for low-quality base calls, with a phred33 < 20 and Illumina adapter sequences using a stringency of 3 with TrimGalore v0.6.5 (104–106). The reads from the T47D cells also included the option --three-Prime-clip-R1 3 in the TrimGalore call. The trimmed reads were then aligned to the *Mus musculus* mm10 or the *Homo sapiens* hg38 genome using Bowtie2 v2.3.4.3 (107). All other processing is as described in "Analysis of *C. elegans* ChIP-seq data" and "Genomic data visualization" sections above.

Protein sequence alignment
Protein sequences were obtained from the National Center for Biotechnology Information (119) and were aligned with Clustal Omega using default settings (120). The alignments were visualized using the Esprit server (121).

Total RNA isolation
Worms were synchronized by bleaching as described above and grown to gravid adulthood on NGM agar plates with OP50-1. To collect late embryos for RNA-seq, the synchronized gravid adults were bleached 60 hours (N2) or 66 hours (*mig-32* and *spat-3* mutants) after release from L1 diapause. Embryos of all genotypes were washed three times in M9/Tx buffer and allowed to develop for 4.5 hours postbleaching in M9/Tx buffer with aeration. The developmental stages of a subset of each sample were scored with differential interference contrast (DIC) microscopy before collection (fig. S11A). TRI Reagent (Sigma-Aldrich) was added to the embryo pellet, followed by 1 to 3 cycles of snap freezing, thawing, and vortexing (1 min). Following chloroform extraction, the aqueous phase was transferred to an RNA Clean and Concentrator-5 column and purified according to the manufacturer's instructions including on-column Dnase I digestion (Zymo Research).

RNA-seq library preparation
PolyA+ RNA was isolated from total RNA using the NEBNext Poly(A) mRNA Magnetic Isolation Module (NEB, E7490) according to the manufacturer's instructions. Libraries were prepared with the NEBNext Ultra II Directional RNA Library Prep with Sample Purification Beads (NEB E7765S) according to the manufacturer's directions with NEBNext Multiplex Oligos for Illumina (NEB E6440).

Library concentration was quantified using NEBNext Library Quant Kit for Illumina (NEB E7630). Pooled libraries were sequenced using NextSeq500 in 75-bp paired-end mode. Details of read counts are in table S2.

Analysis of RNA-seq data
The raw sequencing reads were trimmed as described in "Analysis of *C. elegans* ChIP-seq data" section above. The trimmed reads were then aligned to the *C. elegans* ce11 genome using STAR v2.7.9a (122) with default parameters and filtered for those with MAPQ of 255 with Samtools v1.12 (108). Mapped reads were quantified with Subread v2.0.1's featureCounts (123). Differentially expressed genes were identified with DESeq2 v1.32.0 (124) using a cutoff of $P \leq 0.05$, calculated with the Wald test and corrected for multiple testing using the Benjamini-Hochberg method (125), and a fold change of ≥ 1.5 in either direction. Heatmaps of the normalized counts and $\log_2$ fold changes were prepared with Pheatmap v1.0.12 (116), with "clustering_method" set to "complete" and "clustering_distance_rows" and "clustering_distance_cols" set to "euclidean," or with EnrichedHeatmap v1.22.0 (115), with "clustering_method_rows" set to "ward.D" and clustering_distance_rows set to euclidean. See table S3 for details of wild-type transcript per million counts, $\log_2$ fold changes, and P adjust values for each protein-coding gene in *mig-32* and *spat-3* mutants.

GO analysis
For gene ontology analysis, clusterProfiler v4.0.5 (126) was used to search for enriched biological process terms. For protein-coding genes assigned ChIP-seq peaks, the compareCluster function was used, and the background gene set was defined as all protein-coding genes ($n = 20,094$). For differentially expressed genes, the enrichGO function was used, and the background gene set was defined as all protein-coding genes that were detectable in embryos (raw fragment count of at least 10 in at least one sample, $n = 14,652$). The BioConductor org.Ce.eg.db v3.13.0 database was used, q value cutoff of 0.001, a P value cutoff of 0.001, and pAdjustMethod set to "BH." For protein-coding genes assigned ChIP-seq peaks, the resulting lists were clustered with the findPathClusters function of aPEAR v1.0.0 (68) with similarity set to "jaccard," cluster set to "markov," clusterName set to "pagerank," and minClusterSize set to 8 for genes with only H2AK119ub peaks, 6 for genes with only H3K27me3 peaks, and 5 for genes with H2AK119ub and H3K27me3 peaks. Clusters were visualized with plotPathClusters function of aPEAR (68) with innerCutoff set to 0.1 and outCutoff set to 0.25. For differentially expressed genes and genes with H2AK119ub peaks in N2 and *mig-32(n4275)* mutants, the resulting lists were filtered for redundant terms with clusterProfiler's simplify function, using a similarity threshold of an adjusted P value of 0.7 and the measurement of similarity as described (127) before visualizing. See table S4 for details of enriched GO terms and associated gene lists.

RNAi
For RNAi plates, NGM agar was supplemented with carbenicillin (25 ug/ml) and 5 mM isopropyl-β-D-thiogalactopyranoside. RNAi plates were seeded with *E. coli* HT115 expressing either control double-stranded RNA (dsRNA) (pL4440-Dest; a gift from J. Reece-Hoyes and A. J. M. Walhout, Umass Chan Medical School), *mes-2* dsRNA, or *let-70* dsRNA. The *mes-2* RNAi plasmid (pT444T-mes-2) was constructed by cloning the *mes-2* cDNA into the pL4440 derivative, pT444T [Addgene, plasmid #113081; (128)]. The *let-70* RNAi

plasmid (pT444T-let-70) was constructed by cloning the fragment targeting *let-70* from the Ahringer RNAi library (*129*) into pT444T. RNAi bacteria were grown overnight in LB medium with ampicillin (1000 ug/ml) and diluted to a relative optical density at 600 nm of 2.5 before seeding. Embryos of the P0 generation were grown to gravid adulthood on control or *mes-2* RNAi plates for 73 hours. F1 embryos were isolated by bleaching as described above, allowed to develop for 4 hours and harvested for Western blots. The developmental stages of a subset of the F1 embryos were scored with DIC microscopy. A subset of the F1 embryos was grown to gravid adulthood on RNAi plates for 73 hours and scored for fertility defects. For *let-70* RNAi, animals were grown on control or *let-70* RNAi plates for 48 hours after release from L1 diapause and collected at larval stage L4 for Western blots.

Western blot

Late embryos were prepared as described above (see "Total RNA isolation" section) except that the embryos were harvested 5 hours after bleaching or were harvested as described following RNAi treatment. For staged samples, diapause-arrested L1s were counted and seeded into S-Complete liquid medium (*99*) with OP50-1 as a food source, at a final density of ~0.5 to 1.5 animals/μl. Animals were grown with aeration for 7, 20, 28, or 46.5 hours to larval stage L1, L2, L3, or L4, respectively. Mixed embryos were harvested from adults that were grown with aeration for 71 hours. Early embryos were harvested from adults that were grown with aeration for 61.5 hours. Late embryos were harvested from adults that were grown with aeration for 71 hours but were processed after a further 5 hours of growth. Samples were washed once in resuspension buffer (see "Chromatin immunoprecipitation" section), snap frozen on dry ice in resuspension buffer, and thawed on ice. An equal volume of resuspension buffer with 2× detergents (see "Chromatin immunoprecipitation" section) was added, and samples were sonicated in a Q800R3 water bath sonicator (Qsonica Q800R3-110; 30% power, 15-s on/45-s off) for 2 min. The lysate was centrifuged (13,000g for 15 min at 4°C), and the supernatant was transferred to a new tube. Protein concentration was determined by Bradford assay (Sigma-Aldrich, B6916). Lysates were resolved on a 4 to 12% Bis-tris NuPage gel (Invitrogen), transferred to nitrocellulose, and probed with an anti-H2AK119ub antibody (1:2000; Cell Signaling Technology, rabbit monoclonal D27C4, 8240) or with an anti-H3K27me3 antibody (1:1000; Cell Signaling Technology, rabbit monoclonal C36B11, 9733). The secondary antibody (goat; Cell Signaling Technology, 7074, horseradish peroxidase–conjugated anti-rabbit immunoglobulin G) was used at a dilution of 1:3000. Chemiluminescent signal was visualized using a ChemiDoc MP imaging system (Bio-Rad). Following stripping (15 min in 2% SDS and 0.1 M β-mercaptoethanol preheated to 65°C), blots were reprobed with an anti–histone H3 antibody (1:6000; Abcam, rabbit polyclonal ab1791) as a loading control. Both bands detected by the anti-H2AK119ub antibody are strongly reduced in PRC1 mutants (see Results; Fig. 3A and fig. S7). To provide further evidence that both of these bands are dependent on the ubiquitylation machinery, we used RNAi to knock down *let-70* (ubc-2), the predicted homolog of the E2 ubiquitin–conjugating enzyme human UBE2D1/2/3 based on sequence similarity. The reduction of signal for both the upper and lower band (about 21 and 42%, respectively) (fig. S7C) provides indirect additional support that the epitope recognized by the anti-H2AK119ub antibody is ubiquitin dependent in *C. elegans.*

Supplementary Materials

The PDF file includes:

Figs. S1 to S14
Table S1
Legends for tables S2 to S4
References

Other Supplementary Material for this manuscript includes the following:

Tables S2 to S4

REFERENCES AND NOTES

1. M. I. Kuroda, H. Kang, S. De, J. A. Kassis, Dynamic competition of Polycomb and Trithorax in transcriptional programming. *Annu. Rev. Biochem.* **89**, 235–253 (2020).
2. N. P. Blackledge, A. M. Farcas, T. Kondo, H. W. King, J. F. McGouran, L. L. P. Hanssen, S. Ito, S. Cooper, K. Kondo, Y. Koseki, T. Ishikura, H. K. Long, T. W. Sheahan, N. Brockdorff, B. M. Kessler, H. Koseki, R. J. Klose, Variant PRC1 complex-dependent H2A ubiquitylation drives PRC2 recruitment and Polycomb domain formation. *Cell* **157**, 1445–1459 (2014).
3. A. Scelfo, D. Fernández-Pérez, S. Tamburri, M. Zanotti, E. Lavarone, M. Soldi, T. Bonaldi, K. J. Ferrari, D. Pasini, Functional landscape of PCGF proteins reveals both RING1A/B-dependent-and RING1A/B-independent-specific activities. *Mol. Cell* **74**, 1037–1052.e7 (2019).
4. R. Cao, L. Wang, H. Wang, L. Xia, H. Erdjument-Bromage, P. Tempst, R. S. Jones, Y. Zhang, Role of histone H3 lysine 27 methylation in Polycomb-group silencing. *Science* **298**, 1039–1043 (2002).
5. L. Wang, J. L. Brown, R. Cao, Y. Zhang, J. A. Kassis, R. S. Jones, Hierarchical recruitment of polycomb group silencing complexes. *Mol. Cell* **14**, 637–646 (2004).
6. L. Tavares, E. Dimitrova, D. Oxley, J. Webster, R. Poot, J. Demmers, K. Bezstarosti, S. Taylor, H. Ura, H. Koide, A. Wutz, M. Vidal, S. Elderkin, N. Brockdorff, RYBP-PRC1 complexes mediate H2A ubiquitylation at polycomb target sites independently of PRC2 and H3K27me3. *Cell* **148**, 664–678 (2012).
7. L. Morey, L. Aloia, L. Cozzuto, S. A. Benitah, L. Di Croce, RYBP and Cbx7 define specific biological functions of polycomb complexes in Mouse embryonic stem cells. *Cell Rep.* **3**, 60–69 (2013).
8. Z. Gao, J. Zhang, R. Bonasio, F. Strino, A. Sawai, F. Parisi, Y. Kluger, D. Reinberg, PCGF homologs, CBX proteins, and RYBP define functionally distinct PRC1 family complexes. *Mol. Cell* **45**, 344–356 (2012).
9. N. R. Rose, H. W. King, N. P. Blackledge, N. A. Fursova, K. J. Ember, R. Fischer, B. M. Kessler, R. J. Klose, RYBP stimulates PRC1 to shape chromatin-based communication between Polycomb repressive complexes. *eLife* **5**, e18591 (2016).
10. N. A. Fursova, N. P. Blackledge, M. Nakayama, S. Ito, Y. Koseki, A. M. Farcas, H. W. King, H. Koseki, R. J. Klose, Synergy between variant PRC1 complexes defines polycomb-mediated gene repression. *Mol. Cell* **74**, 1020–1036.e8 (2019).
11. P. Dobrinić, A. T. Szczurek, R. J. Klose, PRC1 drives Polycomb-mediated gene repression by controlling transcription initiation and burst frequency. *Nat. Struct. Mol. Biol.* **28**, 811–824 (2021).
12. I. Cohen, D. Zhao, C. Bar, V. J. Valdes, K. L. Dauber-Decker, M. B. Nguyen, M. Nakayama, M. Rendl, W. A. Bickmore, H. Koseki, D. Zheng, E. Ezhkova, PRC1 fine-tunes gene repression and activation to safeguard skin development and stem cell specification. *Cell Stem Cell* **22**, 726–739.e7 (2018).
13. I. Cohen, C. Bar, H. Liu, V. J. Valdes, D. Zhao, P. M. Galbo, J. M. Silva, H. Koseki, D. Zheng, E. Ezhkova, Polycomb complexes redundantly maintain epidermal stem cell identity during development. *Genes Dev.* **35**, 354–366 (2021).
14. A. Petracovici, R. Bonasio, Distinct PRC2 subunits regulate maintenance and establishment of Polycomb repression during differentiation. *Mol. Cell* **81**, 2625–2639.e5 (2021).
15. H. Sugishita, T. Kondo, S. Ito, M. Nakayama, N. Yakushiji-Kaminatsui, E. Kawakami, Y. Koseki, Y. Ohinata, J. Sharif, M. Harachi, N. P. Blackledge, R. J. Klose, H. Koseki, Variant PCGF1-PRC1 links PRC2 recruitment with differentiation-associated transcriptional inactivation at target genes. *Nat. Commun.* **12**, 5341 (2021).
16. R. Eskeland, M. Leeb, G. R. Grimes, C. Kress, S. Boyle, D. Sproul, N. Gilbert, Y. Fan, A. I. Skoultchi, A. Wutz, W. A. Bickmore, Ring1B compacts chromatin structure and represses gene expression independent of histone ubiquitination. *Mol. Cell* **38**, 452–464 (2010).
17. S. Boyle, I. M. Flyamer, I. Williamson, D. Sengupta, W. A. Bickmore, R. S. Illingworth, A central role for canonical PRC1 in shaping the 3D nuclear landscape. *Genes Dev.* **34**, 931–949 (2020).
18. J. Bonnet, I. Boichenko, R. Kalb, M. Le Jeune, S. Maltseva, M. Pieropan, K. Finkl, B. Fierz, J. Müller, PR-DUB preserves Polycomb repression by preventing excessive accumulation of H2Aub1, an antagonist of chromatin compaction. *Genes Dev.* **36**, 1046–1061 (2022).
19. V. Loubiere, G. L. Papadopoulos, Q. Szabo, A.-M. Martinez, G. Cavalli, Widespread activation of developmental gene expression characterized by PRC1-dependent chromatin looping. *Sci. Adv.* **6**, eaax4001 (2020).

20. H. L. Chan, F. Beckedorff, Y. Zhang, J. Garcia-Huidobro, H. Jiang, A. Colaprico, D. Bilbao, M. E. Figueroa, J. LaCava, R. Shiekhattar, L. Morey, Polycomb complexes associate with enhancers and promote oncogenic transcriptional programs in cancer through multiple mechanisms. *Nat. Commun.* **9**, 3377 (2018).

21. Y. Zhang, T. Liu, F. Yuan, L. Garcia-Martinez, K. D. Lee, S. Stransky, S. Sidoli, R. E. Verdun, Y. Zhang, Z. Wang, L. Morey, The Polycomb protein RING1B enables estrogen-mediated gene expression by promoting enhancer-promoter interaction and R-loop formation. *Nucleic Acids Res.* **49**, 9768–9782 (2021).

22. Y. Zhang, H. L. Chan, L. Garcia-Martinez, D. L. Karl, N. Weich, J. M. Slingerland, R. E. Verdun, L. Morey, Estrogen induces dynamic ERα and RING1B recruitment to control gene and enhancer activities in luminal breast cancer. *Sci. Adv.* **6**, eaaz7249 (2020).

23. D. Desai, P. Pethe, Polycomb repressive complex 1: Regulators of neurogenesis from embryonic to adult stage. *J. Cell. Physiol.* **235**, 4031–4045 (2020).

24. M. Tsuboi, Y. Kishi, W. Yokozeki, H. Koseki, Y. Hirabayashi, Y. Gotoh, Ubiquitination-independent repression of PRC1 targets during neuronal fate restriction in the developing mouse neocortex. *Dev. Cell* **47**, 758–772.e5 (2018).

25. G. Yadirgi, V. Leinster, S. Acquati, H. Bhagat, O. Shakhova, S. Marino, Conditional activation of Bmi1 expression regulates self-renewal, apoptosis, and differentiation of neural stem/progenitor cells in vitro and in vivo. *Stem Cells* **29**, 700–712 (2011).

26. M. Ganapathi, N. C. Boles, C. Charniga, S. Lotz, M. Campbell, S. Temple, R. H. Morse, Effect of Bmi1 over-expression on gene expression in adult and embryonic murine neural stem cells. *Sci. Rep.* **8**, 7464 (2018).

27. X. Gu, X. Wang, D. Su, X. Su, L. Lin, S. Li, Q. Wu, S. Liu, P. Zhang, X. Zhu, X. Jiang, CBX2 inhibits neurite development by regulating neuron-specific genes expression. *Front. Mol. Neurosci.* **11**, 46 (2018).

28. A. Sawai, S. Pfennig, M. Bulajić, A. Miller, A. Khodadadi-Jamayran, E. O. Mazzoni, J. S. Dasen, PRC1 sustains the integrity of neural fate in the absence of PRC2 function. *eLife* **11**, e72769 (2022).

29. H. Eto, Y. Kishi, N. Yakushiji-Kaminatsui, H. Sugishita, S. Utsunomiya, H. Koseki, Y. Gotoh, The Polycomb group protein Ring1 regulates dorsoventral patterning of the mouse telencephalon. *Nat. Commun.* **11**, 5709 (2020).

30. L. A. Doyle, F. Unlu Bektas, E. Chatzantonaki, C. Repton, A. Derrien, R. S. Illingworth, RINGs, DUBs and abnormal brain growth—Histone H2A ubiquitination in brain development and disease. *Epigenomes* **6**, 42 (2022).

31. O. Karakuzu, D. P. Wang, S. Cameron, MIG-32 and SPAT-3A are PRC1 homologs that control neuronal migration in *Caenorhabditis elegans*. *Development* **136**, 943–953 (2009).

32. S. B. Pierce, M. D. Stewart, S. Gulsuner, T. Walsh, A. Dhall, J. M. McClellan, R. E. Klevit, M.-C. King, De novo mutation in RING1 with epigenetic effects on neurodevelopment. *Proc. Natl. Acad. Sci. U.S.A.* **115**, 1558–1563 (2018).

33. G. Bordet, C. Couillault, F. Soulavie, K. Filippopoulou, V. Bertrand, PRC1 chromatin factors strengthen the consistency of neuronal cell fate specification and maintenance in *C. elegans*. *PLOS Genet.* **18**, e1010209 (2022).

34. L. B. Bender, R. Cao, Y. Zhang, S. Strome, The MES-2/MES-3/MES-6 complex and regulation of histone H3 methylation in *C. elegans*. *Curr. Biol.* **14**, 1639–1643 (2004).

35. J. M. Ross, D. Zarkower, Polycomb group regulation of Hox gene expression in *C. elegans*. *Dev. Cell* **4**, 891–901 (2003).

36. T. Yuzyuk, T. H. I. Fakhouri, J. Kiefer, S. E. Mango, The polycomb complex protein *mes-2/E(z)* promotes the transition from developmental plasticity to differentiation in *C. elegans* embryos. *Dev. Cell* **16**, 699–710 (2009).

37. L. J. Gaydos, A. Rechtsteiner, T. A. Egelhofer, C. R. Carroll, S. Strome, Antagonism between MES-4 and Polycomb repressive complex 2 promotes appropriate gene expression in *C. elegans* germ cells. *Cell Rep.* **2**, 1169–1177 (2012).

38. T. Patel, B. Tursun, D. P. Rahe, O. Hobert, Removal of Polycomb repressive complex 2 makes *C. elegans* germ cells susceptible to direct conversion into specific somatic cell types. *Cell Rep.* **2**, 1178–1186 (2012).

39. L. W. Hillier, V. Reinke, P. Green, M. Hirst, M. A. Marra, R. H. Waterston, Massively parallel sequencing of the polyadenylated transcriptome of *C. elegans*. *Genome Res.* **19**, 657–666 (2009).

40. M. E. Boeck, C. Huynh, L. Gevirtzman, O. A. Thompson, G. Wang, D. M. Kasper, V. Reinke, L. W. Hillier, R. H. Waterston, The time-resolved transcriptome of *C. elegans*. *Genome Res.* **26**, 1441–1450 (2016).

41. S. Tamburri, E. Lavarone, D. Fernández-Pérez, E. Conway, M. Zanotti, D. Manganaro, D. Pasini, Histone H2AK119 mono-ubiquitination is essential for polycomb-mediated transcriptional repression. *Mol. Cell* **77**, 840–856.e5 (2020).

42. G. J. Hickey, C. L. Wike, X. Nie, Y. Guo, M. Tan, P. J. Murphy, B. R. Cairns, Establishment of developmental gene silencing by ordered polycomb complex recruitment in early zebrafish embryos. *eLife* **11**, e67738 (2022).

43. L. A. Boyer, K. Plath, J. Zeitlinger, T. Brambrink, L. A. Medeiros, T. I. Lee, S. S. Levine, M. Wernig, A. Tajonar, M. K. Ray, G. W. Bell, A. P. Otte, M. Vidal, D. K. Gifford, R. A. Young, R. Jaenisch, Polycomb complexes repress developmental regulators in murine embryonic stem cells. *Nature* **441**, 349–353 (2006).

44. Y. B. Schwartz, T. G. Kahn, D. A. Nix, X.-Y. Li, R. Bourgon, M. Biggin, V. Pirrotta, Genome-wide analysis of Polycomb targets in *Drosophila melanogaster*. *Nat. Genet.* **38**, 700–705 (2006).

45. T. Liu, A. Rechtsteiner, T. A. Egelhofer, A. Vielle, I. Latorre, M.-S. Cheung, S. Ercan, K. Ikegami, M. Jensen, P. Kolasinska-Zwierz, H. Rosenbaum, H. Shin, S. Taing, T. Takasaki, A. L. Iniguez, A. Desai, A. F. Dernburg, H. Kimura, J. D. Lieb, J. Ahringer, S. Strome, X. S. Liu, Broad chromosomal domains of histone modification patterns in *C. elegans*. *Genome Res.* **21**, 227–236 (2011).

46. J. W. K. Ho, Y. L. Jung, T. Liu, B. H. Alver, S. Lee, K. Ikegami, K.-A. Sohn, A. Minoda, M. Y. Tolstorukov, A. Appert, S. C. J. Parker, T. Gu, A. Kundaje, N. C. Riddle, E. Bishop, T. A. Egelhofer, S. S. Hu, A. A. Alekseyenko, A. Rechtsteiner, D. Asker, J. A. Belsky, S. K. Bowman, Q. B. Chen, R. A.-J. Chen, D. S. Day, Y. Dong, A. C. Dose, X. Duan, C. B. Epstein, S. Ercan, E. A. Feingold, F. Ferrari, J. M. Garrigues, N. Gehlenborg, P. J. Good, P. Haseley, D. He, M. Herrmann, M. M. Hoffman, T. E. Jeffers, P. V. Kharchenko, P. Kolasinska-Zwierz, C. V. Kotwaliwale, N. Kumar, S. A. Langley, E. N. Larschan, I. Latorre, M. W. Libbrecht, X. Lin, R. Park, M. J. Pazin, H. N. Pham, A. Plachetka, B. Qin, Y. B. Schwartz, N. Shoresh, P. Stempor, A. Vielle, C. Wang, C. M. Whittle, H. Xue, R. E. Kingston, J. H. Kim, B. E. Bernstein, A. F. Dernburg, V. Pirrotta, M. I. Kuroda, W. S. Noble, T. D. Tullius, M. Kellis, D. M. MacAlpine, S. Strome, S. C. R. Elgin, X. S. Liu, J. D. Lieb, J. Ahringer, G. H. Karpen, P. J. Park, Comparative analysis of metazoan chromatin organization. *Nature* **512**, 449–452 (2014).

47. N. D. Heintzman, G. C. Hon, R. D. Hawkins, P. Kheradpour, A. Stark, L. F. Harp, Z. Ye, L. K. Lee, R. K. Stuart, C. W. Ching, K. A. Ching, J. E. Antosiewicz-Bourget, H. Liu, X. Zhang, R. D. Green, V. V. Lobanenkov, R. Stewart, J. A. Thomson, G. E. Crawford, M. Kellis, B. Ren, Histone modifications at human enhancers reflect global cell-type-specific gene expression. *Nature* **459**, 108–112 (2009).

48. J. Jänes, Y. Dong, M. Schoof, J. Serizay, A. Appert, C. Cerrato, C. Woodbury, R. Chen, C. Gemma, N. Huang, D. Kissiov, P. Stempor, A. Steward, E. Zeiser, S. Sauer, J. Ahringer, Chromatin accessibility dynamics across *C. elegans* development and ageing. *eLife* **7**, e37344 (2018).

49. A. Vielle, J. Lang, Y. Dong, S. Ercan, C. Kotwaliwale, A. Rechtsteiner, A. Appert, Q. B. Chen, A. Dose, T. Egelhofer, H. Kimura, P. Stempor, A. Dernburg, J. D. Lieb, S. Strome, J. Ahringer, H4K20me1 contributes to downregulation of X-linked genes for *C. elegans* dosage compensation. *PLOS Genet.* **8**, e1002933 (2012).

50. M. B. Wells, M. J. Snyder, L. M. Custer, G. Csankovszki, Caenorhabditis elegans dosage compensation regulates histone H4 chromatin state on X chromosomes. *Mol. Cell. Biol.* **32**, 1710–1719 (2012).

51. M. Kramer, A.-L. Kranz, A. Su, L. H. Winterkorn, S. E. Albritton, S. Ercan, Developmental dynamics of X-chromosome dosage compensation by the DCC and H4K20me1 in *C. elegans*. *PLOS Genet.* **11**, e1005698 (2015).

52. K. Brejc, Q. Bian, S. Uzawa, B. S. Wheeler, E. C. Anderson, D. S. King, P. J. Kranzusch, C. G. Preston, B. J. Meyer, Dynamic control of X chromosome conformation and repression by a Histone H4K20 demethylase. *Cell* **171**, 85–102.e23 (2017).

53. Y. Fong, L. Bender, W. Wang, S. Strome, Regulation of the different chromatin states of autosomes and X chromosomes in the germ line of *C. elegans*. *Science* **296**, 2235–2238 (2002).

54. C. M. Whittle, K. N. McClinic, S. Ercan, X. Zhang, R. D. Green, W. G. Kelly, J. D. Lieb, The genomic distribution and function of histone variant HTZ-1 during *C. elegans* embryogenesis. *PLOS Genet.* **4**, e1000187 (2008).

55. I. Latorre, M. A. Chesney, J. M. Garrigues, P. Stempor, A. Appert, M. Francesconi, S. Strome, J. Ahringer, The DREAM complex promotes gene body H2A.Z for target repression. *Genes Dev.* **29**, 495–500 (2015).

56. A. C. Daugherty, R. W. Yeo, J. D. Buenrostro, W. J. Greenleaf, A. Kundaje, A. Brunet, Chromatin accessibility dynamics reveal novel functional enhancers in *C. elegans*. *Genome Res.* **27**, 2096–2107 (2017).

57. K. J. Evans, N. Huang, P. Stempor, M. A. Chesney, T. A. Down, J. Ahringer, Stable *Caenorhabditis elegans* chromatin domains separate broadly expressed and developmentally regulated genes. *Proc. Natl. Acad. Sci. U.S.A.* **113**, E7020–E7029 (2016).

58. J. Serizay, Y. Dong, J. Jänes, M. Chesney, C. Cerrato, J. Ahringer, Distinctive regulatory architectures of germline-active and somatic genes in *C. elegans*. *Genome Res.* **30**, 1752–1765 (2020).

59. M. P. Creyghton, A. W. Cheng, G. G. Welstead, T. Kooistra, B. W. Carey, E. J. Steine, J. Hanna, M. A. Lodato, G. M. Frampton, P. A. Sharp, L. A. Boyer, R. A. Young, R. Jaenisch, Histone H3K27ac separates active from poised enhancers and predicts developmental state. *Proc. Natl. Acad. Sci. U.S.A.* **107**, 21931–21936 (2010).

60. A. Rada-Iglesias, R. Bajpai, T. Swigut, S. A. Brugmann, R. A. Flynn, J. Wysocka, A unique chromatin signature uncovers early developmental enhancers in humans. *Nature* **470**, 279–283 (2011).

61. V. van den Boom, H. Maat, M. Geugien, A. Rodríguez López, A. M. Sotoca, J. Jaques, A. Z. Brouwers-Vos, F. Fusetti, R. W. J. Groen, H. Yuan, A. C. M. Martens, H. G. Stunnenberg, E. Vellenga, J. H. A. Martens, J. J. Schuringa, Non-canonical PRC1.1 targets active genes independent of H3K27me3 and is essential for leukemogenesis. *Cell Rep.* **14**, 332–346 (2016).

62. A. R. Pengelly, R. Kalb, K. Finkl, J. Müller, Transcriptional repression by PRC1 in the absence of H2A monoubiquitylation. *Genes Dev.* **29**, 1487–1492 (2015).

63. A. L. Jiao, E. Sendinc, B. M. Zee, F. Wallner, Y. Shi, An E2 ubiquitin-conjugating enzyme links diubiquitinated H2B to H3K27M oncohistone function. *Proc. Natl. Acad. Sci. U.S.A.* **121**, e2416614121 (2024).

64. B. Egan, C.-C. Yuan, M. L. Craske, P. Labhart, G. D. Guler, D. Arnott, T. M. Maile, J. Busby, C. Henry, T. K. Kelly, C. A. Tindell, S. Jhunjhunwala, F. Zhao, C. Hatton, B. M. Bryant, M. Classon, P. Trojer, An alternative approach to ChIP-Seq normalization enables detection of genome-wide changes in histone H3 Lysine 27 Trimethylation upon EZH2 inhibition. *PLOS ONE* **11**, e0166438 (2016).

65. R. Kalb, S. Latwiel, H. I. Baymaz, P. W. T. C. Jansen, C. W. Müller, V. Vermeulen, J. Müller, Histone H2A monoubiquitination promotes histone H3 methylation in Polycomb repression. *Nat. Struct. Mol. Biol.* **21**, 569–571 (2014).

66. S. Cooper, M. Dienstbier, R. Hassan, L. Schermelleh, J. Sharif, N. P. Blackledge, P. De Marco, S. Elderkin, H. Koseki, R. Klose, A. Heger, N. Brockdorff, Targeting polycomb to pericentric heterochromatin in embryonic stem cells reveals a role for H2AK119u1 in PRC2 recruitment. *Cell Rep.* **7**, 1456–1470 (2014).

67. A. K. Knutson, A. Rechtsteiner, S. Strome, Reevaluation of whether a soma-to-germ-line transformation extends lifespan in *Caenorhabditis elegans*. *Proc. Natl. Acad. Sci. U.S.A.* **113**, 3591–3596 (2016).

68. I. Kerseviciute, J. Gordevicius, aPEAR: An R package for autonomous visualization of pathway enrichment networks. *Bioinformatics* **39**, btad672 (2023).

69. A. D. Chisholm, H. Hutter, Y. Jin, W. G. Wadsworth, The genetics of axon guidance and axon regeneration in *Caenorhabditis elegans*. *Genetics* **204**, 849–882 (2016).

70. D. Binns, E. Dimmer, R. Huntley, D. Barrell, C. O'Donovan, R. Apweiler, QuickGO: A web-based tool for Gene Ontology searching. *Bioinformatics* **25**, 3045–3046 (2009).

71. A. Jimeno-Martín, E. Sousa, R. Brocal-Ruiz, N. Daroqui, M. Maicas, N. Flames, Joint actions of diverse transcription factor families establish neuron-type identities and promote enhancer selectivity. *Genome Res.* **32**, 459–473 (2022).

72. M. B. Reilly, T. Tekieli, C. Cros, G. R. Aguilar, J. Lao, I. A. Toker, B. Vidal, E. Leyva-Díaz, A. Bhattacharya, S. J. Cook, J. J. Smith, I. Kovacevic, B. Gulez, R. W. Fernandez, E. F. Bradford, Y. H. Ramadan, P. Kratsios, Z. Bao, O. Hobert, Widespread employment of conserved *C. elegans* homeobox genes in neuronal identity specification. *PLOS Genet.* **18**, e1010372 (2022).

73. E. S. Jaensch, J. Zhu, J. C. Cochrane, S. K. Marr, T. A. Oei, M. Damle, E. Z. McCaslin, R. E. Kingston, A Polycomb domain found in committed cells impairs differentiation when introduced into PRC1 in pluripotent cells. *Mol. Cell* **81**, 4677–4691.e8 (2021).

74. S. Cooper, A. Grijzenhout, E. Underwood, K. Ancelin, T. Zhang, T. B. Nesterova, B. Anil-Kirmizitas, A. Bassett, S. M. Kooistra, K. Agger, K. Helin, E. Heard, N. Brockdorff, Jarid2 binds mono-ubiquitylated H2A lysine 119 to mediate crosstalk between Polycomb complexes PRC1 and PRC2. *Nat. Commun.* **7**, 13661 (2016).

75. E. C. Chittock, S. Latwiel, T. C. R. Miller, C. W. Müller, Molecular architecture of polycomb repressive complexes. *Biochem. Soc. Trans.* **45**, 193–205 (2017).

76. V. Kasinath, C. Beck, P. Sauer, S. Poepsel, J. Kosmatka, M. Faini, D. Toso, R. Aebersold, E. Nogales, JARID2 and AEBP2 regulate PRC2 in the presence of H2AK119ub1 and other histone modifications. *Science* **371**, eabc3393 (2021).

77. M. Almeida, G. Pintacuda, O. Masui, Y. Koseki, M. Gdula, A. Cerase, D. Brown, A. Mould, C. Innocent, M. Nakayama, L. Schermelleh, T. B. Nesterova, H. Koseki, N. Brockdorff, PCGF3/5-PRC1 initiates Polycomb recruitment in X chromosome inactivation. *Science* **356**, 1081–1084 (2017).

78. D. Colognori, H. Sunwoo, A. J. Kriz, C.-Y. Wang, J. T. Lee, Xist deletional analysis reveals an interdependency between xist RNA and polycomb complexes for spreading along the inactive X. *Mol. Cell* **74**, 101–117.e10 (2019).

79. Z. Chen, M. N. Djekidel, Y. Zhang, Distinct dynamics and functions of H2AK119ub1 and H3K27me3 in mouse preimplantation embryos. *Nat. Genet.* **53**, 551–563 (2021).

80. H. Mei, C. Kozuka, R. Hayashi, M. Kumon, H. Koseki, A. Inoue, H2AK119ub1 guides maternal inheritance and zygotic deposition of H3K27me3 in mouse embryos. *Nat. Genet.* **53**, 539–550 (2021).

81. J. M. Gahan, F. Rentzsch, C. E. Schnitzler, The genetic basis for PRC1 complex diversity emerged early in animal evolution. *Proc. Natl. Acad. Sci. U.S.A.* **117**, 22880–22889 (2020).

82. A. L. Saltzman, M. W. Soo, R. Aram, J. T. Lee, Multiple histone methyl-lysine readers ensure robust development and germline immortality in *Caenorhabditis elegans*. *Genetics* **210**, 907–923 (2018).

83. B. de Potter, M. W. D. Raas, M. F. Seidl, C. P. Verrijzer, B. Snel, Uncoupled evolution of the Polycomb system and deep origin of non-canonical PRC1. *Commun. Biol.* **6**, 1144 (2023).

84. J. A. Zepeda-Martinez, C. Pribitzer, J. Wang, D. Bsteh, S. Golumbeanu, Q. Zhao, T. R. Burkard, B. Reichholf, S. K. Rhie, J. Jude, H. F. Moussa, J. Zuber, O. Bell, Parallel PRC2/cPRC1 and vPRC1 pathways silence lineage-specific genes and maintain self-renewal in mouse embryonic stem cells. *Sci. Adv.* **6**, eaax5692 (2020).

85. D. J. Grau, B. A. Chapman, J. D. Garlick, M. Borowsky, N. J. Francis, R. E. Kingston, Compaction of chromatin by diverse Polycomb group proteins requires localized regions of high charge. *Genes Dev.* **25**, 2210–2221 (2011).

86. M. Leeb, D. Pasini, M. Novatchkova, M. Jaritz, K. Helin, A. Wutz, Polycomb complexes act redundantly to repress genomic repeats and genes. *Genes Dev.* **24**, 265–276 (2010).

87. S. Strome, W. G. Kelly, S. Ercan, J. D. Lieb, Regulation of the X chromosomes in *Caenorhabditis elegans*. *Cold Spring Harb. Perspect. Biol.* **6**, a018366 (2014).

88. U. Grossniklaus, R. Paro, Transcriptional silencing by polycomb-group proteins. *Cold Spring Harb. Perspect. Biol.* **6**, a019331 (2014).

89. A. Barral, J. Déjardin, The chromatin signatures of enhancers and their dynamic regulation. *Nucleus* **14**, 2160551 (2023).

90. M. Uckelmann, C. Davidovich, Chromatin compaction by Polycomb group proteins revisited. *Curr. Opin. Struct. Biol.* **86**, 102806 (2024).

91. E. Yemini, A. Lin, A. Nejatbakhsh, E. Varol, R. Sun, G. E. Mena, A. D. T. Samuel, L. Paninski, V. Venkatachalam, O. Hobert, NeuroPAL: A multicolor atlas for whole-brain neuronal identification in *C. elegans*. *Cell* **184**, 272–288.e11 (2021).

92. R. Godini, H. Fallahi, R. Pocock, The regulatory landscape of neurite development in *Caenorhabditis elegans*. *Front. Mol. Neurosci.* **15**, 974208 (2022).

93. F. Chiacchiera, A. Rossi, S. Jammula, A. Piunti, A. Scelfo, P. Ordóñez-Morán, J. Huelsken, H. Koseki, D. Pasini, Polycomb complex PRC1 preserves intestinal stem cell identity by sustaining Wnt/β-Catenin transcriptional activity. *Cell Stem Cell* **18**, 91–103 (2016).

94. J. E. Sulston, Neuronal cell lineages in the nematode *Caenorhabditis elegans*. *Cold Spring Harb. Symp. Quant. Biol.* **48**, 443–452 (1983).

95. A. V. Molofsky, R. Pardal, T. Iwashita, I.-K. Park, M. F. Clarke, S. J. Morrison, Bmi-1 dependence distinguishes neural stem cell self-renewal from progenitor proliferation. *Nature* **425**, 962–967 (2003).

96. D. Zencak, M. Lingbeek, C. Kostic, M. Tekaya, E. Tanger, D. Hornfeld, M. Jaquet, F. L. Munier, D. F. Schorderet, M. van Lohuizen, Y. Arsenijevic, Bmi1 loss produces an increase in astroglial cells and a decrease in neural stem cell population and proliferation. *J. Neurosci.* **25**, 5774–5783 (2005).

97. M. Román-Trufero, H. R. Méndez-Gómez, C. Pérez, A. Hijikata, Y. Fujimura, T. Endo, H. Koseki, C. Vicario-Abejón, M. Vidal, Maintenance of undifferentiated state and self-renewal of embryonic neural stem cells by Polycomb protein Ring1B. *Stem Cells* **27**, 1559–1570 (2009).

98. M. Yao, X. Zhou, J. Zhou, S. Gong, G. Hu, J. Li, K. Huang, P. Lai, G. Shi, A. P. Hutchins, H. Sun, H. Wang, H. Yao, PCGF5 is required for neural differentiation of embryonic stem cells. *Nat. Commun.* **9**, 1463 (2018).

99. T. Stiernagle, Maintenance of *C. elegans*. *WormBook*, 1–11 (2006).

100. S. Brenner, The genetics of *Caenorhabditis elegans*. *Genetics* **77**, 71–94 (1974).

101. S. Ercan, P. G. Giresi, C. M. Whittle, X. Zhang, R. D. Green, J. D. Lieb, X chromosome repression by localization of the *C. elegans* dosage compensation machinery to sites of transcription initiation. *Nat. Genet.* **39**, 403–408 (2007).

102. A. Rechtsteiner, S. Ercan, T. Takasaki, T. M. Phippen, T. A. Egelhofer, W. Wang, H. Kimura, J. D. Lieb, S. Strome, The histone H3K36 methyltransferase MES-4 acts epigenetically to transmit the memory of germline gene expression to progeny. *PLOS Genet.* **6**, e1001091 (2010).

103. P. Askjaer, S. Ercan, P. Meister, Modern techniques for the analysis of chromatin and nuclear organization in *C. Elegans*. *WormBook*, 1–35 (2014).

104. S. Andrews, FastQC: A quality control tool for high throughput sequence data (2010).

105. M. Martin, Cutadapt removes adapter sequences from high-throughput sequencing reads. *EMBnet. J.* **17**, 10–12 (2011).

106. F. Krueger, TrimGalore: A wrapper tool around Cutadapt and FastQC to consistently apply quality and adapter trimming to FastQ files (2015).

107. B. Langmead, S. L. Salzberg, Fast gapped-read alignment with Bowtie 2. *Nat. Methods* **9**, 357–359 (2012).

108. H. Li, B. Handsaker, A. Wysoker, T. Fennell, J. Ruan, N. Homer, G. Marth, G. Abecasis, R. Durbin, 1000 Genome Project Data Processing Subgroup, The Sequence Alignment/Map format and SAMtools. *Bioinformatics* **25**, 2078–2079 (2009).

109. Y. Zhang, T. Liu, C. A. Meyer, J. Eeckhoute, D. S. Johnson, B. E. Bernstein, C. Nusbaum, R. M. Myers, M. Brown, W. Li, X. S. Liu, Model-based analysis of ChIP-seq (MACS). *Genome Biol.* **9**, R137 (2008).

110. H. M. Amemiya, A. Kundaje, A. P. Boyle, The ENCODE Blacklist: Identification of problematic regions of the genome. *Sci. Rep.* **9**, 9354 (2019).

111. A. R. Quinlan, I. M. Hall, BEDTools: A flexible suite of utilities for comparing genomic features. *Bioinformatics* **26**, 841–842 (2010).

112. P. V. Kharchenko, M. Y. Tolstorukov, P. J. Park, Design and analysis of ChIP-seq experiments for DNA-binding proteins. *Nat. Biotechnol.* **26**, 1351–1359 (2008).

113. F. Ramírez, F. Dündar, S. Diehl, B. A. Grüning, T. Manke, deepTools: A flexible platform for exploring deep-sequencing data. *Nucleic Acids Res.* **42**, W187–W191 (2014).

114. G. Yu, L.-G. Wang, Q.-Y. He, ChIPseeker: An R/Bioconductor package for ChIP peak annotation, comparison and visualization. *Bioinformatics* **31**, 2382–2383 (2015).

115. Z. Gu, R. Eils, M. Schlesner, N. Ishaque, EnrichedHeatmap: An R/Bioconductor package for comprehensive visualization of genomic signal associations. *BMC Genomics* **19**, 234 (2018).

116. R. Kolde, pheatmap: Pretty Heatmaps, R package version 1.0.12, version 1.0.12 (2019); https://CRAN.R-project.org/package=pheatmap.

117. W. J. Kent, C. W. Sugnet, T. S. Furey, K. M. Roskin, T. H. Pringle, A. M. Zahler, D. Haussler, The human genome browser at UCSC. *Genome Res.* **12**, 996–1006 (2002).

118. R. Edgar, M. Domrachev, A. E. Lash, Gene Expression Omnibus: NCBI gene expression and hybridization array data repository. *Nucleic Acids Res.* **30**, 207–210 (2002).

119. E. W. Sayers, E. E. Bolton, J. R. Brister, K. Canese, J. Chan, D. C. Comeau, R. Connor, K. Funk, C. Kelly, S. Kim, T. Madej, A. Marchler-Bauer, C. Lanczycki, S. Lathrop, Z. Lu, F. Thibaud-Nissen, T. Murphy, L. Phan, Y. Skripchenko, T. Tse, J. Wang, R. Williams, B. W. Trawick, K. D. Pruitt, S. T. Sherry, Database resources of the National Center for Biotechnology Information. *Nucleic Acids Res.* **50**, D20–D26 (2022).

120. F. Sievers, A. Wilm, D. Dineen, T. J. Gibson, K. Karplus, W. Li, R. Lopez, H. McWilliam, M. Remmert, J. Söding, J. D. Thompson, D. G. Higgins, Fast, scalable generation of high-quality protein multiple sequence alignments using Clustal Omega. *Mol. Syst. Biol.* **7**, 539 (2011).

121. X. Robert, P. Gouet, Deciphering key features in protein structures with the new ENDscript server. *Nucleic Acids Res.* **42**, W320–W324 (2014).

122. A. Dobin, C. A. Davis, F. Schlesinger, J. Drenkow, C. Zaleski, S. Jha, P. Batut, M. Chaisson, T. R. Gingeras, STAR: Ultrafast universal RNA-seq aligner. *Bioinformatics* **29**, 15–21 (2013).

123. Y. Liao, G. K. Smyth, W. Shi, featureCounts: An efficient general purpose program for assigning sequence reads to genomic features. *Bioinformatics* **30**, 923–930 (2014).

124. M. I. Love, W. Huber, S. Anders, Moderated estimation of fold change and dispersion for RNA-seq data with DESeq2. *Genome Biol.* **15**, 550 (2014).

125. Y. Benjamini, Y. Hochberg, Controlling the false discovery rate: A practical and powerful approach to multiple testing. *J. R. Stat. Soc. B. Methodol.* **57**, 289–300 (1995).

126. G. Yu, L.-G. Wang, Y. Han, Q.-Y. He, clusterProfiler: An R package for comparing biological themes among gene clusters. *OMICS* **16**, 284–287 (2012).

127. J. Z. Wang, Z. Du, R. Payattakool, P. S. Yu, C.-F. Chen, A new method to measure the semantic similarity of GO terms. *Bioinformatics* **23**, 1274–1281 (2007).

128. Á. Sturm, É. Saskoi, K. Tibor, N. Weinhardt, T. Vellai, Highly efficient RNAi and Cas9-based auto-cloning systems for *C. elegans* research. *Nucleic Acids Res.* **46**, e105 (2018).

129. R. S. Kamath, J. Ahringer, Genome-wide RNAi screening in *Caenorhabditis elegans*. *Methods* **30**, 313–321 (2003).

130. M. V. Rockman, L. Kruglyak, Recombinational landscape and population genomics of *Caenorhabditis elegans*. *PLOS Genet.* **5**, e1000419 (2009).

131. R. K. McGinty, R. C. Henrici, S. Tan, Crystal structure of the PRC1 ubiquitylation module bound to the nucleosome. *Nature* **514**, 591–596 (2014).

132. ENCODE Project Consortium, An integrated encyclopedia of DNA elements in the human genome. *Nature* **489**, 57–74 (2012).